NASA CONTRACTOR REPORT

EXPERIMENTAL INVESTIGATION OF THE EFFECT OF GENERAL IMPERFECTIONS ON THE BUCKLING OF CYLINDRICAL SHELLS

by Johann Arbocz and C. D. Babcock, Jr.

Prepared by
CALIFORNIA INSTITUTE OF TECHNOLOGY
Pasadena, Calif.
for

NATIONAL AERONAUTICS AND SPACE ADMINISTRATION • WASHINGTON, D. C. • SEPTEMBER 1968

NASA CR-1163

EXPERIMENTAL INVESTIGATION OF THE EFFECT OF GENERAL IMPERFECTIONS ON THE BUCKLING OF CYLINDRICAL SHELLS

By Johann Arbocz and C. D. Babcock, Jr.

Prepared under Grant No. NsG-18-59 by
CALIFORNIA INSTITUTE OF TECHNOLOGY
Pasadena, Calif.

for

NATIONAL AERONAUTICS AND SPACE ADMINISTRATION

For sale by the Clearinghouse for Federal Scientific and Technical Information
Springfield, Virginia 22151 – CFSTI price $3.00

ACKNOWLEDGMENT

The authors wish to express their sincere appreciation to Dr. E. E. Sechler for his guidance of the work carried out in this investigation. The advice and suggestions of other members of the Department of Aeronautics, especially of Dr. William Supple is also appreciated. They also want to thank, for the help received throughout the course of experimental study, Mr. George Carlson of the Aeronautics Shop and Mr. Marvin Jessey of the Electronics Laboratory. Very much appreciated was the help of Miss Helen Burrus for the typing and of Mrs. Betty Wood for the graphs and figures.

This study was supported in part by the National Aeronautics and Space Administration under Research Grant Nsg 18-59 and this aid is gratefully acknowledged.

TABLE OF CONTENTS

TABLE OF CONTENTS (Cont'd)

LIST OF SYMBOLS

E	Young's Modulus
t	Shell thickness
L	Length of the shell
ν	Poisson's Ratio
ξ	Nondimensional imperfection amplitude
ξ_I	Nondimensional initial imperfection amplitude
A_{ij}	Coefficient of $\cos i\bar{x} \cdot \cos j\bar{y}$
B_{ij}	Coefficient of $\cos i\bar{x} \cdot \sin j\bar{y}$
C_{ij}	Coefficient of $\sin i\bar{x} \cdot \cos j\bar{y}$
D_{ij}	Coefficient of $\sin i\bar{x} \cdot \sin j\bar{y}$
η	Nondimensional number indicating size of imperfection growth
Δ_i	Growth of initial imperfection after application of the ith load increment (in per cent of thickness)
$\bar{w}(x, y)$	Radial imperfection from perfect circular cylinder
x, y	Axial and circumferential coordinates on middle surface of shell, respectively
$\bar{x}, \bar{y}$	Nondimensional coordinates ($\bar{x} = \frac{2\pi x}{L}$, $\bar{y} = \frac{y}{R}$)
X_1, Y_1	Coordinates locating origin of the best fit cylinder reference axis
ϵ_1, ϵ_2	Small angles in Radians denoting the inclination of the best fit cylinder reference axis ($\epsilon_1 = \pi/2 - \alpha$; $\epsilon_2 = \pi/2 - \beta$ when using notation of Fig. 20)
R	Radius of the best fit cylinder
m	Number of waves in the circumferential directions

EXPERIMENTAL INVESTIGATION OF THE EFFECT OF GENERAL IMPERFECTIONS ON THE BUCKLING OF CYLINDRICAL SHELLS

By Johann Arbocz and C. D. Babcock, Jr.

ABSTRACT

In the past several investigators have analytically shown that the marked decrease from the theoretical load carrying capacity of cylindrical shells under axial compression observed in practice could be attributed to geometrical imperfections of the shells.

This paper presents the first known results of complete imperfection surveys carried out on cylindrical shells before and during the loading process up to the buckling load.

A non-contact probe has been used to make these surveys on electroformed copper shells. The data recording process has been fully automatized and the data reduction was done on an IBM 7094. Three-dimensional plots were obtained of the measured initial imperfection surfaces and of the growth of these imperfections under increasing axial loading. The modal components of the measured imperfection surfaces were also obtained.

Preliminary results indicated that the prebuckling deformation which apparently caused the reduction in buckling load from that of a perfect shell could not be represented by an isolated mode.

I. INTRODUCTION

In the last decade geometrical imperfections have come to be accepted as one of the main degrading factors in the load carrying capacity of cylindrical shells under axial compression. Since the paper by Donnell and Wan in 1950 there have been many refinements in the theoretical approaches (Refs. 1, 2, 3, and 4). Experimental studies, however, seem to have suffered under the very difficult task of accurately recording imperfections of the order of only fractions of the wall thicknesses.

The purpose of the test series reported in this paper was to determine the effect of imperfections on the buckling load of cylindrical shells under axial compression by carrying out complete imperfection surveys on the cylindrical shells before and during the loading process up to the buckling load. Also by tracing the growth of the initial imperfections during the loading process prior to buckling it was hoped to isolate those modal components which furnished the mechanism by which the initial imperfections reduced the buckling load.

The following sections contain a description of the instrumentation designed to carry out these tests. An outline of the check-out procedures used to assure the proper functioning of the individual components is also included.

II. THE PROGRAM

1. Test Equipment

a. Traversing Mechanism

The specifications of the experimental program called for a scanning device that would be adequate to pick-up and record imperfections of only fractions of the test specimen's wall thickness of 0.004 inch. In addition the scanning device had to travel both in the axial and in the circumferential directions in order to record a complete surface map of the shell being tested. The numbers(1), (2) etc. used in the following section refer to part numbers listed in Fig. 1.

The scanning device was built around an inductance-type, noncontacting pick-up which measured the air gap between the end of the pick-up and the conducting copper surface of the shell. The pick-up was installed in a support(3) which in turn was fixed to a long shaft(2) protruding inside the shell being tested. The 22 inch long, 1-3/8 inch diameter stainless steel shaft was ground on a cylindrical grinder to a straightness of less than 0.0001 inch total indicator reading. Also its deviation from roundness was kept to less than 0.000025 inch total indicator reading. This shaft was supported by two bronze bearings, which were pressed into an aluminum alloy supporting ring(1) and then lapped to fit the shaft. For better adjustment, the

bronze bearings were partially split and could be tightened or loosened by fine thread set screws. The shaft could be moved axially in and out by means of a leadscrew(5) which was supported in a self-aligning bearing(66) pressed into the end-piece(4). This in turn, was supported by the outer shell(12) consisting of a 5 inch diameter aluminum alloy tube. The leadscrew was driven by the axial motor(72) installed on the rear plate(17) of the end-cap(16). The shaft was driven in the circumferential direction by the circumferential motor(71) installed at the rear side of a supporting plate(6) which traveled back and forth with the shaft in the axial direction. Whenever the shaft was driven in the circumferential direction the axial drive had to be disengaged in order to avoid moving the shaft axially because of the advancing or retreating nut on the leadscrew. The disengagement was accomplished by de-energizing a magnetic coupling(70). The circumferential position of the pick-up was determined by the print control consisting of a microswitch which was triggered by the switching disk(9) which had 48 uniformly spaced notches machined into it. The traversing sequence which consisted of a circumferential scan followed by an axial advance was controlled by strategically spaced microswitches. It will be described in more detail in the section on the Model Control Unit. Figure 1 shows the assembly drawing of the traversing mechanism, Fig. 2 shows the scanning mechanism unassembled and Fig. 3 shows the assembled scanning device.

In the following sections the supporting electronic equipment will be described. Figure 4 shows an overall layout of the system as a whole.

b. Model Control Unit

As mentioned earlier, during the imperfection measurements the shaft of the traversing device supporting the noncontact probe was driven alternatingly in the axial and circumferential directions by small electric motors. The control of this automatic sequence was accomplished by a series of relays controlled by microswitches. Figure 5 shows the general layout of the model control unit. To start the automatic scanning sequence the shaft had to be in the home position.

Only then did pressing of the start button energize relay(2). Energizing the relay made power available to the circumferential motor which started rotating the shaft in the counter clockwise direction. At the same time relay(6) was energized opening the clutch between the axial motor and the leadscrew. This was necessary because otherwise the rotational motion of the shaft would result in a simultaneous axial advance. Upon completing its circumferential scan, the circular cam riding on the shaft tripped one of the circumferential limit switches. This stopped the circumferential motor, de-energized relay(6) which engaged the clutch between the axial motor and the leadscrew. At the same time relay(2) was also de-energized creating a pulse that operated relay(3), that latched relay(4), making power available to the axial motor which started advancing the shaft of the scanning device. Upon completing the preset axial advance the incremental switch was tripped stopping the axial motor and deactivating relay(4). This resulted in a pulse on relay(1), which latched relay(2). The latching of relay(2) started the circumferential motor in the clockwise direction, and the whole sequence was repeated. The automatic scanning with intermittent circumferential scans and axial advances continued until the shaft completed its full axial advance tripping the upper axial limit switch which stopped the sequence. The circumferential and the axial position of the noncontact probe was monitored by the output of two helipots. One helipot was driven by the circumferential motion, the other by the axial motion of the shaft respectively. The output of the circumferential position indicator helipot was also used to drive the x-axis of the xy-plotter used to record the pick-up signal directly on the y-axis of the graph paper.

The control of the traversing device could also be switched from automatic to manual. Then the circumferential and axial motion were controlled by separate 3 position switches eliminating the automatic sequencing. The completion of a full circumferential scan, or the full travel in the axial direction was determined by the limit switches.

c. Pick-up System

The pick-up circuit shown on Fig. 6 consisted of two inductance-type pick-ups, an oscillator, a differential amplifier and a demodulator. The pick-ups consisted of a coil with a powdered iron core excited by a 100 KH_z signal generated by the oscillator. The impedance of the coils to this signal changed as their electromagnetic fields were disturbed by the eddy currents generated in the external conducting surfaces. The dummy pick-up was preset during the calibration of the active pick-up and its setting remained the same for any given test. By determining the change in impedance of the coil of the active pick-up the position of the external shell surface could be measured quite accurately. This was done by first amplifying the voltage across the active pick-up's coil 100 times on the differential amplifier, then demodulating this AC signal. The output of the demodulator, consisting of a DC voltage was then read on the digital voltmeter and recorded on cards by an IBM 526 card punch. Using the dummy pick-up and the differential amplifier increased the sensitivity of the system to 1.0 volt per 0.001 inches as compared to a sensitivity of 0.25 volt per 0.001 inches if the active pick-up was used alone.

d. Data Control Unit

As can be seen from the experimental set-up in Fig. 4, the same digital voltmeter was used to read the strain gages on the load cell and the demodulated DC signal of the pick-up used to measure the imperfections of the test shell. To control the sequence of the signals fed to the digital voltmeter, a data control unit was built which included a 26 channel stepping switch circuit. Twenty-four channels were connected to the strain gages on the load cell, the 25th channel indicated the voltage of the power source used to energize the strain gage circuits, the 26th channel was the home position. It read the demodulated DC signal of the imperfection measuring pick-up. Using the stepping switch made it possible to read the strain gages automatically at a preset rate. Channel 26 of the data control unit also included an adjustable time delay circuit. This circuit became

necessary because of the finite sampling time required by the Cimron digital voltmeter. Thus when using channel 26 the punch signal from the circular cam trapped the output of the pick-up at that particular instant in the time delay circuit. This would allow time enough for the digital voltmeter to sample this signal and to come to an essentially constant reading. At the end of the preset time delay the circuit activated the card punch recording the last reading of the digital voltmeter.

e. Digital Voltmeter

The digital voltmeter used for the tests was made by Cimron Division of Lear Siegler Inc., Trademark Cimron, Model P9400B with a DC preamplifier mode 6812B. Balance time for a full scale change in the 5 digits was 300 milliseconds.

f. Card Punch

The recording of the data was done on an IBM 526 card punch with a capability of 15 characters per second. The format used to record the data was 9F8.4 with the last 8 columns used to record the run number and the card number. The run number was dialed in through a parameter board and the number of cards used was monitored on a card counter connected to the card punch.

2. Check-out of the Test Equipment

a. Scans of Known Contours

In checking out the pick-up system, at first a surface of known contour was scanned with the pick-up and its output was recorded by the DVM card punch system, giving the recorded data in terms of voltages. Later it was converted into displacements on an IBM 7094 by means of the pick-up's calibration curve. The shape of the contour obtained by the pick-up measurements was then cross-plotted with the shape of the contour as measured very accurately on an optical comparator. Figure 7 shows a cross-plot of pick-up measurements vs. optical comparator measurements. The agreement between the two readings was excellent except for the regions adjacent to the sharp step where the pick-up measurements deviated from the exact shape due to the integrating feature of the pick-up. The width of this region was approximately equal to the diameter of the pick-up.

Since the scanning of the shells with the pick-up was to be done continuously it was necessary to verify that the output of the digital voltmeter, which was recorded in set intervals automatically on cards, represented the true shape of the measured shell surface. The verification was done by scanning a carefully machined surface of known contour with the pick-up moving at constant speed and recording the output of the pick-up by the DVM card punch system. A sample of this data is shown in Fig. 8. The agreement between the pick-up measurements and the measurements made with a micrometer was once again very good except for the regions close to sharp corners where the integrating property of the pick-up smoothened out the shape of the scanned surface.

b. Circumferential Time Delay Check-Out

During the circumferential scans a circular cam rotating with the shaft triggered a microswitch at every 7.5° (See Fig. 1 for details). This was the signal to the Model Control Unit to record the readings of the Digital Voltmeter on cards by the IBM card punch. The intermittent counterclockwise and clockwise circumferential motion resulted initially in misalignments of identical circumferential stations measured at different axial positions. This was caused by the fact that the circular cam triggered the microswitch at different positions depending upon whether it was moving clockwise of counterclockwise. This problem was solved by placing an adjustable time delay into the punch control circuit. Figure 9 explains in detail the triggering sequence with and without the time delay.

Proper adjustment of the time delay circuit was achieved with the help of an xy-plotter. The x-axis was driven by the circumferential position indicator helipot, whereas the y-axis was connected across the punch relay. Thus every punch was registered as a square wave on the graph paper. Using the graphs of the counterclockwise and clockwise scans done side by side the deviations from the planned exact punch locations were read off without any difficulty. Figure 10 shows a picture of the counterclockwise and clockwise punch signals, whereas Fig. 11 shows the computed deviations from the planned exact punch locations. It was possible to hold the punch intervals as $7.5^{\circ} \pm 0.5^{\circ}$.

c. Hysteresis and Repeatability of the Measured Data

For the checkout of the system as a whole a thick-walled aluminum cylinder was used. This cylinder was machined out of standard thick-walled aluminum tubing and was precision honed so that its deviations from roundness and its deviations from the mean diameter combined were less than 0.0005 in. total indicator reading.

Basically it should not have mattered whether the circumferential scanning at any one axial station was done clockwise or counterclockwise. However due to friction in the bronze bearings and play in the overall mechanical system it was expected that a certain amount of hysteresis would exist between the counterclockwise and clockwise scans at any one axial station. Figure 12 shows plots of the pick-up output during counterclockwise and clockwise circumferential scans at three different axial stations. The maximum deviation at any one point between the clockwise and counterclockwise scans was less than 0.0003 inch, for most part of the plot less than 0.0001 inch. It should be remarked here that originally, before making the bronze bearings adjustable the hysteresis between the clockwise and counterclockwise outputs was of the order of 0.001 inch.

The final checkout of the system as a whole consisted of the complete surface scan of the near perfect thick-walled aluminum cylinder. The data was punched on cards, ran through the data reduction program and it was found that the maximum amplitude of any one of the computed harmonics was less than 0.0006 inch. This was in good agreement with the previously mentioned tolerances of fabrication of this cylinder.

This complete surface scan was repeated at a later date and the reduced data compared with the results of the first scan. Repeatability was found to be very good. Table I gives some data on these measurements.

3. Fabrication of the Test Specimen

The cylindrical shells used for this testing program were fabricated by electroforming on wax mandrels. This process was used previously in other investigations (Ref. 2). About an inch thick

layer of wax was first cast on water cooled mandrels. After the wax had hardened it was machined to the desired dimensions on a lathe and spray painted with a silver paint thinned with Toluene. The plating was carried out in a Copper Fluoborate bath. Because of previous experience, copper was retained as the plating material. The plating time was about 20 minutes per 0.001 inches of plate. After the plating was completed, the mandrel was rinsed thoroughly and the shell cut to the desired length while it was still on the mandrel. After the cutting operation the shell was then removed from the mandrel by melting out the wax. The excess wax and silver paint was removed from the finished shells with benzene. For a more detailed description of the plating process see references 2 and 5.

a. Wall Thickness

The average thickness of the test shells was determined before the buckling tests by weighing the shells. The specific gravity used in the calculation of the thickness was 8.9. The thickness variation along the generator of the shells was determined by cutting strips out of the first test specimens and determining their thickness by a comparator. The thickness variation was found to be less than $\pm$ 2.5 per cent of the nominal value (See also Ref. 2).

b. Material Properties

Tests to determine the material properties of the plated copper were carried out in uniaxial tension. This was done by utilizing long strips of the plated copper which were soldered into 1/8 inch thick plates that were in turn clamped into the jaws of an Instron testing machine. The strips had length to width ratios of about 80. The head displacement of the testing machine was used as the measure of strain and the load read from the Instron load cell. The results of the tests are shown in Table II.

A determination of Poisson's ratio for each shell was not attempted since its influence in the reduction of the buckling data is of secondary importance. A value of 0.3 was used for this purpose.

4. Test Procedure

The buckling tests were carried out in the controlled end-displacement type testing machine shown in Fig. 13. By the use of matched pairs of high precision thrust bearings the axial elastic displacement under load of the testing machine was kept to a minimum thus making the testing machine rigid in comparison with the test specimen. The relative displacement of the two end plates of the testing machine was controlled by four loading screws, which could be adjusted independently to give the proper load distribution on the shell, or simultaneously to increase the load up to the critical value. One complete turn of the screws gave a displacement of 0.025 inches. Figure 14 shows the details of these displacement controlling screws. The springs shown in Fig. 13 were used to preload the testing machine when installing the test specimen in the machine and securing it to the upper end plate of the testing machine. The testing was carried out when the machine was in the position shown in Fig. 13. The end plate with the gear drive rested on pins and the opposite end rested on a set of rollers. By this arrangement the frictional torque produced when turning the gears was transmitted through the pins into the base plate on which the testing machine rested, and the test specimen was loaded by axial compression only.

a. Load Cell

During the buckling tests the load distribution was monitored and the total load was obtained by means of the load cell shown in Fig. 15. It consisted of a seamless, electroformed copper cylinder which was 0.015 inches thick, 3.00 inches long and 8.00 inches in diameter. Twenty-four foil type strain gages from Micro-Measurements Inc., Serial No. MA-09-500BH-120 with extra stable characteristics were mounted on the cylinder equally spaced around the circumference. The ones on the inside were directly opposite to those on the outside. It has been shown in reference 2 that the strain measured by this type of arrangement represented very accurately the actual strain in the test shell. The load cell was secured to the end plate of the testing machine with a thin layer of Devcon. Devcon is a plastic-like material in a putty state which hardens in several hours after the addition of a hardening agent.

b. Calibration of the Pick-up

To carry out the imperfection measurements the traversing mechanism was installed in the position shown in Fig. 16 with the shaft protruding through the hole in the end-plate inside the load cell. To carry out the calibration of the pick-up which was installed in a movable support at the end of the protruding shaft, a short shell was cast with Cerrolow into the load cell as shown in Fig. 16. Then the pick-up was moved vertically away from the surface of the shell 0.001 inch at the time recording the reading of the digital voltmeter each time. Figure 17 shows a typical calibration curve with the working range and the preset position of the pick-up so indicated. Upon completion of the calibration the pick-up was preset to a position about at the center of the working range. Next the shaft was retracted into the load cell, the short calibration shell was removed and the load cell was ready for the installment of the test shell.

c. Installing the Test Shell

The test shell was fastened into an end ring with a low melting point alloy Cerrolow and its other end was secured to the load cell in the same manner. After this operation was completed the end ring was secured to the upper end-plate by a thin layer of Devcon. Upon hardening of the Devcon the cylinder was ready for testing. Figure 18 shows the complete cylindrical shell testing configuration.

d. Initial Imperfection Measurements

After the installment of the test specimen into the testing machine was completed a full automatic imperfection scan of the shell was performed. The data was recorded both by the IBM card punch and by the xy-plotter. The imperfection measurements on the shells A7, A8, and A9 were carried out with a pick-up 5/8" in diameter. Because of the integrating properties of the pick-up the axial increments were preset to be 1/2". The initial axial station was 1/2" from that end of the shell which was cast into the load cell. The automatic scanning sequence was started with a counterclockwise circumferential scan at the initial axial station followed by an axial advance of 1/2". This was followed by a clockwise circumferential

scan and the automatic sequence continued with intermittent axial advances and circumferential scans until the full length of the shell was covered. In this test series the shells were 8 inches long, so 14 axial advances of 1/2 inches each were used. The last axial station was 1/2 inches from the upper end of the shell. Upon completion of the initial imperfection measurements the shaft of the scanning device was run back to its initial position, designated also as home position.

e. *Monitoring of the Strain Gages*

Before carrying out the buckling tests the gages on the load cell were connected to a 24 channel bridge box which contained 24 Wheatstone bridge circuits. In order to minimize the effect of temperature changes an additional 24 strain gages were installed on a dummy cylinder and connected to the same bridge box where they formed one of the branches of the individual Wheatstone bridge circuits. The initial zero reading could be adjusted individually through differential shunt balances. The output of the bridge was monitored by a Cimron Digital Voltmeter. By using the stepping switch unit connected between the bridge and the digital voltmeter the readings of the 24 strain gages were recorded automatically by means of an IBM card punch. The total compressive load was computed by averaging the readings of all gages and using a previously determined calibration factor. The calibration of the load cell was carried out using a very accurate Schaevitz dynamometer-type load ring.

f. Buckling Procedure

Upon completion of the initial imperfection measurements the cylindrical shells were initially loaded to about one-sixth of the expected buckling load and the circumferential load distribution was made as uniform as possible by individually adjusting the four loading screws of the testing machine. This was followed by another complete automatic scanning of the shell surface. The duration of an automatic scan was about 1/2 hour. The strain gages were read before and after the completion of the scan and the load was taken as the average of the two readings. The axial load was then increased in small increments by turning the four loading screws simultaneously. After each loading

the load distribution was adjusted again. Also after each load increment another complete scan of the shell surface was performed. Thus any change in the shell surface due to the increase in loading was recorded. This was carried out up to about two-thirds of the expected buckling load. After this point the load distribution was no longer adjusted so as to prevent buckling occurring during one of the adjustments. The load was increased in small increments, each load increment followed by a complete scan of the shell surface and the strain gages were monitored until buckling occurred. It should be noted here that due to the working range of 0.125 inches of the pick-up used for the imperfection measurements, it was possible to get a complete scan of the postbuckling shapes of the shells tested.

5. Data Reduction - Main Program

As described in the previous sections the imperfection measurements were carried out by scanning the surface of the test shells by an inductance-type pick-up. The output of the pick-up was monitored on a digital voltmeter whose readings were recorded at preset intervals by an IBM 526 card punch on cards. Thus, upon completion of each buckling test, there was a set of cards containing the displacement pick-up calibration data in volts and displacements and a set of cards containing the shell displacements given in volts for each scan completed. These displacements were referred to the end of the pick-up. The shell displacements were given in volts because they consisted of the readings of the digital voltmeter recorded at preset intervals.

The data reduction of the experimental measurements was done on an IBM 7094 digital computer. Figure 19 shows a flow chart of the main data reduction program. By using an overlay technique it could handle up to 29 x 97 = 2813 experimental points.

a. Best Fit Polynomial to Pick-up Calibration Data

The first step in the data reduction program consisted of fitting a best fit polynomial of the form

$$\delta = \sum_{n=o}^{N} a_n V^n$$

to the working range of the pick-up's calibration data. Figure 17 shows the calibration data of the pick-up used on shell A7 and the corresponding best fit polynomial curve.

The unknown coefficients a_n of the polynomial representation were determined by the Method of Least Squares and stored in a common block for later use. As a measure of the accuracy of the best fit approximation, the χi-squared error was also computed. It was found that the best possible approximation, that is the approximation for which the χi-squared error was the least, was obtained for N = 16.

Next the data reduction program converted the voltage readings of the initial imperfection scan into displacements in inches using the polynomial representation of the calibration curve obtained in the previous step. These displacements were also stored in a common block for later use.

Upon completing the conversion of the data of the initial imperfection scan link[1] was erased from the core except for the results stored in common blocks.

b. Definition of the "Perfect" Cylinder

In the experimental set up shown in Fig. 1 a certain misalignment of the shell center line with that of the traversing device was expected. Thus it was necessary to remove from the measured imperfection data the effects of such a misalignment. Also before the harmonic components of the measured imperfection surface could be computed it was necessary to define what was considered the perfect shell. This was accomplished by finding the best fit cylinder to the data of the initial imperfection scan. This was done by the Method of Least Squares by first computing the sum of the squares of the normal distances from the measured points in space to the surface of the assumed best fit cylinder.

$$S = \sum_{i=1}^{N} d_i^2 = \sum_{i=1}^{N} (R_i - R)^2 = f(X_1, Y_1, \epsilon_1, \epsilon_2, R)$$

(See Fig. 20)

Minimizing S with respect to the unknown parameters $X_1, Y_1, \epsilon_1, \epsilon_2$ and R yielded then five simultaneous, nonlinear algebraic equations

in the five unknowns. Assuming that $X_1, Y_1, \epsilon_1, \epsilon_2$ were small, these equations were linearized and then solved to determine the new reference axis system and to define the perfect cylinder. See Fig. 20.

In link(2) the data reduction program computed $X_1, Y_1, \epsilon_1, \epsilon_2$, R and stored them in a common block. Next it took the measured displacements reduced by link(1) which originally were referred to the end of the scanning pick-up from the common block and recomputed them with respect to the newly found best fit cylinder of radius R. Then the measured displacements, which now represented deviations from the perfect cylinder, were stored in the same common block. Upon completion of this step, link(2) was erased from the core except for the results stored in common blocks.

c. Finding the Harmonic Components of the Measured Imperfection Surface

Three different Fourier representations were used for the measured imperfection surfaces. The full wave representation in the axial direction involved the determination of four sets of harmonic components:

$$\overline{w}(x,y) = \sum_{m=o}^{N}\sum_{n=o}^{N} A_{mn} \cos m\frac{y}{R} \cos\frac{2n\pi x}{L} +$$

$$\sum_{m=1}^{N}\sum_{n=o}^{N} B_{mn} \sin m\frac{y}{R} \cos\frac{2n\pi x}{L} +$$

$$\sum_{m=o}^{N}\sum_{n=1}^{N} C_{mn} \cos m\frac{y}{R} \sin\frac{2n\pi x}{L} + \sum_{m=1}^{N}\sum_{n=1}^{N} D_{mn} \sin m\frac{y}{R} \sin\frac{2n\pi x}{L}$$

where

$$A_{mn} = \frac{2}{\pi L} \int_0^L \int_0^{2\pi R} \overline{w}(x, y) \cos m \frac{y}{R} \cos \frac{2n\pi x}{L} \, dy \, dx$$

$$B_{mn} = \frac{2}{\pi L} \int_0^L \int_0^{2\pi R} \overline{w}(x, y) \sin m \frac{y}{R} \cos \frac{2n\pi x}{L} \, dy \, dx$$

$$C_{mn} = \frac{2}{\pi L} \int_0^L \int_0^{2\pi R} \overline{w}(x, y) \cos m \frac{y}{R} \sin \frac{2n\pi x}{L} \, dy \, dx$$

$$D_{mn} = \frac{2}{\pi L} \int_0^L \int_0^{2\pi R} \overline{w}(x, y) \sin m \frac{y}{R} \sin \frac{2n\pi x}{L} \, dy \, dx$$

The half wave cosine representation in the axial direction involved the determination of two sets of harmonic components:

$$\overline{w}(x, y) = \sum_{m=o}^{N} \sum_{n=o}^{N} A_{mn} \cos m \frac{y}{R} \cos \frac{n\pi x}{L} + \sum_{m=1}^{N} \sum_{n=o}^{N} B_{mn} \sin m \frac{y}{R} \cos \frac{n\pi x}{L}$$

where

$$A_{mn} = \frac{1}{\pi L} \int_{-L}^{L} \int_0^{2\pi R} \overline{w}(x, y) \cos m \frac{y}{R} \cos \frac{n\pi x}{L} \, dy \, dx$$

$$B_{mn} = \frac{1}{\pi L} \int_{-L}^{L} \int_0^{2\pi R} \overline{w}(x, y) \sin m \frac{y}{R} \cos \frac{n\pi x}{L} \, dy \, dx$$

Finally the half wave sine representation in the axial direction also involved the determination of two sets of harmonic components:

$$\overline{w}(x, y) = \sum_{m=o}^{N} \sum_{n=1}^{N} C_{mn} \cos m \frac{y}{R} \sin \frac{n\pi x}{L} + \sum_{m=1}^{N} \sum_{n=1}^{N} D_{mn} \sin m \frac{y}{R} \sin \frac{n\pi x}{L}$$

where

$$C_{mn} = \frac{1}{\pi L} \int_{-L}^{L} \int_{0}^{2\pi R} \overline{w}(x, y) \cos m \frac{y}{R} \sin \frac{n\pi x}{L} \, dy \, dx$$

$$D_{mn} = \frac{1}{\pi L} \int_{-L}^{L} \int_{0}^{2\pi R} \overline{w}(x, y) \sin m \frac{y}{R} \sin \frac{n\pi x}{L} \, dy \, dx$$

Separate subroutines were written for the different Fourier representations. The double integrals involved in the determination of the required coefficients were carried out numerically using the trapesoidal rule. Before returning to the main program each subroutine not only printed out the computed Fourier coefficients but also punched them on cards. In addition, upon return to the main program, the measured displacements representing the deviations from the defined perfect cylinder were printed out and punched on cards.

After the data reduction of the initial imperfection measurements was completed the program returned to read in the data of the second full scan. The data reduction of the second full scan and of all the subsequent full scans was done using the polynomial representation of the pick-up calibration obtained during the data reduction of the initial imperfection scan. However the position of the best fit cylinder and with it the definition of the perfect cylinder were recomputed for each scan.

Thus upon completion of the data reduction of the buckling test of a shell by the layered main program the following output has been obtained:

1. A list of the location of the best fit or perfect shell at each load level.

2. The measured shell displacements representing deviations from the perfect shell at each load level both listed and punched on cards.

3. The coefficients of any one of the three Fourier representations at each load level both listed and punched on cards.

6. Data Reduction - Auxiliary Programs

The output from the main data reduction program was examined in different ways.

a. Three-Dimensional Plots

The cards containing the measured deviations from the perfect shell at different load levels were used as the input to a plotting program. When the proper values were assigned to the built in flags this program prepared three-dimensional plots of the imperfection scans at different load levels by offsetting the origin of the successive circumferential scans by the proper amount along both the x- and y-axis. The same program was also used to prepare three-dimensional plots of the growth of imperfections at increasing load levels. This was done by subtracting from the measured shell surface at each load level the measured initial imperfections of the shell before calling the plotting subroutine.

b. Computing the Growth of Harmonic Components

The cards containing the computed coefficients of the chosen Fourier representation of the measured shell surfaces at each load level were used as the input to an auxiliary program, that computed the growth of each of the coefficients with increasing loading. This was done by subtracting from the coefficients at each load level the corresponding coefficients from the initial scan.

7. Test Results

As stated in the introduction the purpose of this experimental study was to determine the effect of initial imperfections on the buckling load of cylindrical shells under axial compression and to find the

mechanism by which imperfections reduce the load carrying capacity of the shells. The instrumentation was designed and built to detect such initial imperfections and to trace their growth during the loading process prior to buckling. The results of buckling test on three cylindrical shells are reported here.

By using electroformed copper shells seamless test specimens of great uniformity were obtained. The wall thickness was constant to within $\pm$ 2 per cent. By adjusting the four loading screws individually during the buckling test variation in the load distribution around the circumference of the shells was kept to within $\pm$ 10 $^{o}/o$. Detailed results of the buckling tests for these shells are summarized in Table II. By using electroformed copper shells it was felt that the size of the unintended initial imperfections would be minimized. However all three shells had initial imperfections that were greater than the wall thicknesses of the respective shells as can be seen from Fig. 21 through Fig. 23 which show the initial surveys of shells A7, A8, and A9. The principal Fourier coefficients of the initial surveys are summarized in Table III. Table IV shows the variation of the "perfect" cylinder with load increments for the shells A7, A8 and A9. Figures 24 through 26 show the growth of the prebuckling deformation of shell A7 after the first load increment, at $P/P_{c\ell} = 0.061$ and after the last load increment prior to local buckling. Figures 27 through 32 show the growth of the prebuckling deformation of the shells A8 and A9 after the first load increment, at $P/P_{c\ell} = 0.047$ for shell A8 at $P/P_{c\ell} = 0.042$ for shell A9 and after the last load increment prior to buckling. Figure 33 shows the local buckling pattern of shell A7. Figures 34 through 36 show the post-buckling patterns of the shells A7, A8 and A9 respectively.

The local buckling of shell A7 consisted of two isolated waves as can be seen on Fig. 33. The location of these initial buckles coincided with the most pronounced growth of the prebuckling deformation just prior to the occurrence of the local buckling as shown on Fig. 26. The location of these initial buckles also coincided with the location of very pronounced localized defects in the test specimen as can be seen from the initial scan of shell A7, shown in Fig. 21. These

localized waves caused the load distribution to fall off in their neighborhood without appreciably affecting the distribution over the rest of the circumference of the shell. After the initial local buckling the load was increased until general collapse occurred without attempting to adjust the load distribution. General collapse occurred in the same manner as for the other two shells A8 and A9 but at a lower value of axial loading than expected. Shell A8 and A9 did not have an initial local buckling.

General collapse consisted of a snap-through which is characteristic of this type of test. In all cases the post-buckling state consisted of 2 to 3 rows of buckles that extended completely around the circumference. The number of circumferential waves is noted in Table II.

As stated previously, the load distribution was adjusted to be as uniform as possible with the four loading screws of the testing machine. The adjustment was done by equalizing the strain in the load cell at the 45°, 135°, 225° and 315° position. This adjustment was not attempted after about 75 per cent of the expected buckling load was obtained. Table II gives the maximum variation in load distribution near buckling. Figure 37 shows the load distribution on the three shells at the last reading before buckling.

The three-dimensional plots representing the growth of the prebuckling deformations showed at a glance the general deformation pattern of the shell before buckling. As seen from Fig. 24 through Fig. 32 there was a very pronounced growth of an imperfection whose half wave length in the axial direction was approximately equal to the length of the shell. The number of circumferential waves of this predominant imperfection mode was approximately equal to the number of circumferential waves in the post-buckled shape. However, the wave length in the axial direction in the post-buckled shape was considerably shorter than the length of the shells as can be seen from Figs. 34 through 36.

In an attempt to isolate the "critical modal components", defined as those modal components which showed exponential growth close to the critical load, harmonic analysis of the measured imperfection

surfaces were carried out at each load level. For each complete scan approximately 700 Fourier coefficients were calculated to describe the measured shell surfaces. Both full wave and half wave axial representations were used. About 25 of the computed Fourier coefficients showed significant growth rate. Figure 38 through Fig. 40 show the growth rate of three such coefficients for shell A7, A8, and A9 respectively. As can be seen from these figures the curves representing the experimentally measured growth rates approach a horizontal tangent at the experimental buckling load. The same characteristic curves were obtained for other coefficients. However, most of the coefficients that approach a horizontal tangent at the experimental buckling load were close in circumferential and axial wave numbers. All the coefficients that were investigated are summarized in Table V.

III. CONCLUSION

Due to the small number of shells tested the results obtained thus far must be considered only preliminary. However the following conclusions seemed to be warranted:

1. The initial imperfections of the shells surveyed so far were characterized by being composed predominantly of lower order modes (i.e. few circumferential and axial waves). The amplitudes of the higher order modes were in general very small (i.e. of the order of 1 $^{o}/o$ of the wall thickness or less). (See also Table III).

2. As can be seen from the three-dimensional plots representing the growth of the prebuckling deformations (Fig. 24 through Fig. 32) there was a very pronounced growth of imperfection components with long axial wave length and short circumferential wave length for all three shells tested. The number of circumferential waves of these dominant components was approximately equal to the number of circumferential waves in the postbuckled shape. The half wave length of the dominant components was equal to the length of the shell in the axial direction. However the axial half wave length of the postbuckled

shape was much shorter than the axial half wave length of the dominant components in the prebuckling deformation.

3. There seemed to exist several "critical modal components" for every shell tested all showing the same exponential growth close to the critical load instead of an isolated "critical modal component". In other words the mode of prebuckling deformation which apparently contributed to the reduction in buckling load of the shells had many Fourier coefficients. Furthermore, some of these components had relatively small initial values. That is, the "critical modal components" were not necessarily predominant in the initial imperfection shape.

4. The failure mode of shell A7 with local buckling in two isolated waves seemed to support the claim expressed in other publications (See Ref. 5) that local bucklings were caused by some pronounced localized initial imperfections of the test specimen. Upon comparing the local buckling pattern of shell A7 (Fig. 33) with the initial imperfection survey of the same shell (Fig. 21) it was strikingly evident that not only did the initial local buckling occur at the exact location of very pronounced localized initial defects of the test specimen but the same localized defects showed the most pronounced growth rate at different load levels as can be seen from Fig. 26 just prior to the occurrence of local buckling.

REFERENCES

1. Donnell, L. H., and Wan, C. C.: Effect of Imperfections on Buckling of Thin Cylinders and Columns under Axial Compression. Journal Appl. Mech., Vol. 17, No. 1, p. 73 (1950).
2. Babcock, C. D.: The Buckling of Cylindrical Shells with an Initial Imperfection under Axial Compression Loading. Ph. D. Thesis, California Institute of Technology (1962).
3. Koiter, W. T.: Elastic Stability and Post Buckling Behaviour. Proc. Symposium on Non-Linear Problems, edited by R. E. Langer, University of Wisconsin Press, Madison, Wisconsin (1963).
4. Thurston, G. A. and Freeland, M. A.: Buckling of Imperfect Cylinders under Axial Compression. NASA CR-541 (1966).
5. Arbocz, J.: Buckling of Conical Shells under Axial Compression. GALCIT Report SM 68-6, California Institute of Technology, February 1968.

TABLE I

REPEATABILITY CHECKS

Date of Scan	$X_1 \cdot 10^2$	$Y_1 \cdot 10^2$	$\epsilon_1 \cdot 10^3$	$\epsilon_2 \cdot 10^3$	R
	Inches	Inches	Radians	Radians	Inches
9-21-67	0.15626	-0.51015	0.14259	-1.0810	3.9921
9-22-67-10:00 am	0.15574	-0.50604	0.14174	-1.0754	3.9919
9-22-67-5:00 pm	0.15822	-0.50609	0.14059	-1.0750	3.9919
Average Value	$0.15674 \pm 1\%$	$-0.50743 \pm 0.5\%$	$0.14164 \pm 0.7\%$	$-1.0771 \pm 0.3\%$	3.99197

TABLE I (Cont'd)

REPEATABILITY CHECKS

Date of Scan	$A_{1,0} \cdot 10^4$	$A_{2,0} \cdot 10^3$	$A_{1,1} \cdot 10^3$	$B_{2,0} \cdot 10^4$	$C_{2,1} \cdot 10^3$
	Inches	Inches	Inches	Inches	Inches
9-21-67	-0.111382	0.582548	0.108452	0.337139	-0.149562
9-22-67-10:00 am	-0.106870	0.570465	0.112480	0.339966	-0.158353
9-22-67-5:00 pm	-0.117174	0.572949	0.114902	0.404532	-0.158584
Average Value	$-0.111811 \pm 5\%$	$0.575321 \pm 1.3\%$	$0.111945 \pm 0.5\%$	$0.360546 \pm 10\%$	$-0.155500 \pm 4\%$

TABLE II

SUMMARY OF BUCKLING TESTS

Shell	$E \times 10^{-6}$ lb/in^2	$t \times 10^3$ inches	$\frac{P}{P_{c\ell}}$	$\frac{\sigma_{max} - \sigma_{min}}{\sigma_{ave}}$ %	m	Remarks
A7	15.1	4.494	0.553/0.597	28.9	13	Local Buckling with 2 isolated dimples in the middle
A8	15.2	4.640	0.658	22.0	13	
A9	14.7	4.540	0.736	17.0	13	

For all 3 shells: R = 4.00 inches, L = 8.25 inches

TABLE III

PRINCIPAL COMPONENTS OF THE INITIAL IMPERFECTION SURFACE

Shell A-7		Shell A-8		Shell A-8 (Cont'd)		Shell A-9	
	$\xi \cdot 10^{-2}$ (% of t)		$\xi \cdot 10^{-2}$ (% of t)		$\xi \cdot 10^{-2}$ (% of t)		$\xi \cdot 10^{-2}$ (% of t)
$A_{2,0}$	-0.40171	$A_{2,0}$	-0.61127	$A_{0,7}$	-0.07160	$A_{2,0}$	-0.15274
$A_{3,0}$	-0.45609	$A_{3,0}$	0.65505	$B_{2,0}$	0.23677	$A_{3,0}$	0.15427
$A_{4,0}$	0.10324	$A_{4,0}$	0.12821	$B_{6,0}$	0.09854	$A_{6,0}$	-0.07760
$A_{5,0}$	0.19307	$A_{6,0}$	0.08617	$C_{0,1}$	0.61062	$B_{2,0}$	0.44998
$A_{6,0}$	0.11413	$A_{7,0}$	0.13751	$C_{0,2}$	0.26611	$B_{3,0}$	-0.24033
$B_{2,0}$	-0.24141	$A_{0,1}$	0.10266	$C_{0,4}$	0.07517	$B_{4,0}$	0.16388
$B_{3,0}$	0.14999	$A_{0,2}$	-0.19917	$B_{2,1}$	0.06527	$B_{5,0}$	0.07567
$B_{4,0}$	0.50396	$A_{0,3}$	-0.07959	$C_{3,1}$	0.06120	$B_{7,0}$	-0.08599
$B_{5,0}$	0.12837	$A_{0,4}$	-0.08128	$C_{4,1}$	-0.17972	$C_{0,1}$	0.69449
$B_{6,0}$	-0.16509	$A_{0,5}$	-0.06254	$C_{5,1}$	0.10175	$C_{2,1}$	-0.18336
$B_{7,0}$	-0.74003	$A_{0,6}$	-0.06369	$C_{2,2}$	0.29195	$C_{3,1}$	-0.11512

TABLE III (Cont'd)

PRINCIPAL COMPONENTS OF THE INITIAL

IMPERFECTION SURFACE

Shell A-7 (Cont'd)	$\xi \cdot 10^{-2}$ (% of t)	Shell A-8 (Cont'd)	$\xi \cdot 10^{-2}$ (% of t)	Shell A-8 (Cont'd)	$\xi \cdot 10^{-2}$ (% of t)	Shell A-9 (Cont'd)	$\xi \cdot 10^{-2}$ (% of t)
$C_{0,1}$	0.06827	$C_{2,3}$	-0.10536	$D_{4,1}$	-0.11285	$C_{4,1}$	0.07458
$C_{4,2}$	-0.06428	$C_{5,2}$	0.07173	$D_{2,2}$	-0.06762	$C_{2,2}$	-0.09209
$D_{2,6}$	-0.06327	$D_{2,1}$	-0.22114	$D_{3,2}$	-0.07252	$D_{2,1}$	-0.31208
$D_{3,2}$	-0.07913	$D_{3,1}$	0.08688			$D_{2,2}$	-0.14532
						$D_{2,3}$	-0.08739

Note: $\xi = \frac{\text{Amplitude of the Harmonic}}{\text{Wall Thickness}}$

TABLE IV

VARIATION OF THE BEST FIT ("PERFECT") CYLINDER

WITH LOAD INCREMENTS

A7		$\frac{P}{P_{c\ell}}$ %	$X_1 \cdot 10^2$ Inches	$Y_1 \cdot 10^2$ Inches	$\epsilon_1 \cdot 10^2$ Radians	$\epsilon_2 \cdot 10^2$ Radians	R Inches
1		-3.9	-0.501	-0.055	-0.218	0.120	4.0047
2		6.1	-0.504	-0.054	-0.217	0.119	4.0046
3		11.0	-0.502	-0.053	-0.219	0.119	4.0048
4		18.8	-0.506	-0.052	-0.219	0.118	4.0048
5		23.0	-0.511	-0.050	-0.221	0.119	4.0049
6		27.0	-0.523	-0.041	-0.219	0.118	4.0051
7		32.5	-0.516	-0.040	-0.220	0.118	4.0053
8		38.2	-0.517	-0.039	-0.219	0.118	4.0054
9		45.1	-0.513	-0.039	-0.221	0.118	4.0059
10		53.9	-0.520	-0.041	-0.223	0.118	4.0060
11	**	55.3	-0.485	-0.035	-0.222	0.118	4.0058
12	*	59.7	-0.271	0.107	-0.271	0.065	4.0040

* Buckling Pattern

** Initial Local Buckling Pattern

TABLE IV (Cont'd)

VARIATION OF THE BEST FIT ("PERFECT") CYLINDER

WITH LOAD INCREMENTS

A8	$\frac{P}{P_{c\ell}}$ %	$X_1 \cdot 10^2$ Inches	$Y_1 \cdot 10^2$ Inches	$\epsilon_1 \cdot 10^2$ Radians	$\epsilon_2 \cdot 10^2$ Radians	R Inches
1	-2.4	-0.757	0.304	-0.266	0.109	4.0036
2	4.7	-0.766	0.307	-0.265	0.110	4.0033
3	11.0	-0.776	0.318	-0.267	0.111	4.0034
4	20.5	-0.782	0.325	-0.268	0.111	4.0034
5	27.4	-0.782	0.325	-0.269	0.112	4.0034
6	33.9	-0.784	0.324	-0.270	0.112	4.0034
7	42.0	-0.784	0.323	-0.270	0.111	4.0035
8	48.5	-0.786	0.322	-0.271	0.111	4.0036
9	56.4	-0.788	0.321	-0.271	0.110	4.0037
10	63.7	-0.789	0.321	-0.271	0.110	4.0038
11	*65.8	-0.789	0.286	-0.269	0.108	4.0010

* Buckling Pattern

TABLE IV (Cont'd)

VARIATION OF THE BEST FIT ("PERFECT") CYLINDER

WITH LOAD INCREMENTS

A9	$\frac{P}{P_{c\ell}}$ %	$X_1 \cdot 10^2$ Inches	$Y_1 \cdot 10^2$ Inches	$\epsilon_1 \cdot 10^2$ Radians	$\epsilon_2 \cdot 10^2$ Radians	R Inches
1	-4.5	-0.594	0.346	-0.213	0.101	4.0007
2	4.2	-0.599	0.348	-0.210	0.100	4.0007
3	11.8	-0.602	0.349	-0.210	0.100	4.0009
4	20.9	-0.603	0.350	-0.209	0.101	4.0010
5	28.6	-0.604	0.352	-0.209	0.101	4.0012
6	36.0	-0.605	0.353	-0.209	0.101	4.0012
7	43.5	-0.605	0.353	-0.209	0.101	4.0012
8	50.4	-0.605	0.354	-0.208	0.101	4.0012
9	57.1	-0.607	0.355	-0.207	0.101	4.0015
10	61.4	-0.605	0.355	-0.208	0.102	4.0015
11	65.6	-0.605	0.355	-0.209	0.102	4.0016
12	69.1	-0.604	0.354	-0.209	0.101	4.0016
13	72.2	-0.604	0.353	-0.209	0.101	4.0015
14	*73.6	-0.680	0.307	-0.210	0.102	3.9989

* Buckling Pattern

TABLE V

SUMMARY OF "CRITICAL" FOURIER COEFFICIENTS

Shell A-7	$\Delta_9 \cdot 10^{-2}$ (% of t)	$\xi_1 \cdot 10^{-2}$ (% of t)	η
$A_{2,0}$	0.0555	-0.4017	-0.13
$A_{6,0}$	-0.0149	0.1141	-0.13
$A_{9,0}$	0.0260	0.0307	0.85
$A_{12,0}$	0.0113	0.0053	2.14
$B_{2,0}$	-0.0235	-0.2414	0.10
$B_{6,0}$	-0.0114	-0.1651	0.07
$B_{7,0}$	0.0188	-0.0740	-0.25
$B_{13,0}$	-0.0176	-0.02635	0.67
$C_{0,1}$	-0.0446	0.0683	-0.65
$C_{0,2}$	-0.0156	0.01307	-1.19
$A_{9,1}$	-0.0199	-0.02818	0.71
$A_{10,1}$	0.0120	0.02875	0.42
$A_{18,2}$	-0.0117	-0.0060	1.95
$B_{1,1}$	-0.0114	0.0125	-0.91
$B_{13,1}$	0.0162	0.0347	0.47
$B_{15,1}$	-0.0106	-0.0129	0.82
$C_{8,1}$	0.0119	-0.0331	-0.36
$C_{11,1}$	0.0164	0.0328	0.50
$C_{15,1}$	0.0242	0.0158	1.53
$D_{11,1}$	0.0154	0.0361	0.43
$D_{12,1}$	-0.0220	-0.0363	0.61
$D_{14,1}$	0.0328	0.0195	1.68

TABLE V (Cont'd)

SUMMARY OF "CRITICAL" FOURIER COEFFICIENTS

Shell A-8	$\Delta_9 \cdot 10^{-2}$ (°/o of t)	$\xi_1 \cdot 10^{-2}$ (°/o of t)	η
$A_{2,0}$	-0.0233	-0.6113	0.04
$A_{5,0}$	0.0131	-0.0383	-0.34
$A_{8,0}$	-0.0242	0.0058	-4.16
$A_{12,0}$	0.0144	-0.0023	-6.26
$A_{13,0}$	0.0242	-0.0184	-1.31
$A_{0,1}$	0.0126	0.1027	0.12
$B_{2,0}$	-0.0264	0.0237	-1.11
$B_{3,0}$	-0.0204	-0.0422	0.48
$B_{8,0}$	-0.0119	-0.0448	0.27
$B_{10.0}$	0.0131	-0.0541	-0.24
$B_{12,0}$	-0.0283	0.0040	-7.08
$B_{13,0}$	0.0137	0.0071	1.93
$C_{0,1}$	0.0110	0.6106	0.018
$A_{8,1}$	0.0116	0.0244	0.48
$A_{12,1}$	-0.0132	-0.0069	1.91
$A_{13,1}$	-0.0241	-0.0230	1.05
$B_{12,1}$	0.0227	0.0132	1.72
$B_{13,1}$	-0.0115	-0.0155	0.74
$B_{16,1}$	-0.0108	-0.0033	3.28

TABLE V (Cont'd)

SUMMARY OF "CRITICAL" FOURIER COEFFICIENTS

Shell A-8	$\Delta_9 \cdot 10^{-2}$ (°/o of t)	$\xi_1 \cdot 10^{-2}$ (°/o of t)	η
$C_{9,1}$	-0.0106	0.0041	-2.59
$C_{10,1}$	0.0159	0.0149	1.03
$D_{4,1}$	0.0132	-0.1129	-0.12
$D_{9,1}$	-0.0110	-0.0483	0.23
$D_{11,1}$	0.0196	0.0116	1.69
$D_{14,1}$	0.0111	-0.0093	-1.20

TABLE V (Cont'd)

SUMMARY OF "CRITICAL" FOURIER COEFFICIENTS

Shell A-9	$\Delta_9 \cdot 10^{-2}$ (% of t)	$\xi_1 \cdot 10^{-2}$ (% of t)	η
$A_{8,0}$	-0.0197	-0.0043	4.58
$A_{9,0}$	-0.0382	-0.0609	0.63
$A_{10,0}$	-0.0259	-0.0012	21.58
$A_{11,0}$	-0.0227	-0.0015	15.15
$B_{6,0}$	-0.0151	-0.0045	3.36
$B_{10,0}$	0.0153	-0.0050	- 3.06
$C_{0,1}$	-0.0128	0.0694	- 0.18
$A_{1,1}$	0.0166	0.0074	2.24
$A_{9,1}$	0.0274	0.0221	1.24
$A_{10,1}$	0.0146	0.0150	0.97
$A_{11,1}$	0.0234	0.0146	1.60
$A_{13,1}$	0.0128	0.0044	2.91
$A_{14,1}$	0.0141	0.0045	3.14
$B_{13,1}$	-0.0187	-0.0081	2.31
$B_{15,1}$	-0.0110	0.0022	- 5.00
$B_{16,1}$	-0.0121	-0.0092	1.32
$B_{16,2}$	0.0106	0.0024	4.42
$B_{18,2}$	0.0103	0.0003	34.40

TABLE V (Cont'd)

SUMMARY OF "CRITICAL" FOURIER COEFFICIENTS

Shell A-9	$\Delta_9 \cdot 10^{-2}$ (% of t)	$\xi_1 \cdot 10^{-2}$ (% of t)	η
$C_{2,1}$	0.0106	-0.1833	- 0.06
$C_{12,1}$	-0.0295	-0.0307	0.96
$C_{14,1}$	-0.0142	-0.0022	6.45
$C_{15,1}$	-0.0112	-0.0056	2.00
$D_{10,1}$	-0.0106	-0.0209	0.50
$D_{12,1}$	-0.0246	0.0126	- 1.95
$D_{13,1}$	-0.0180	-0.0178	1.01

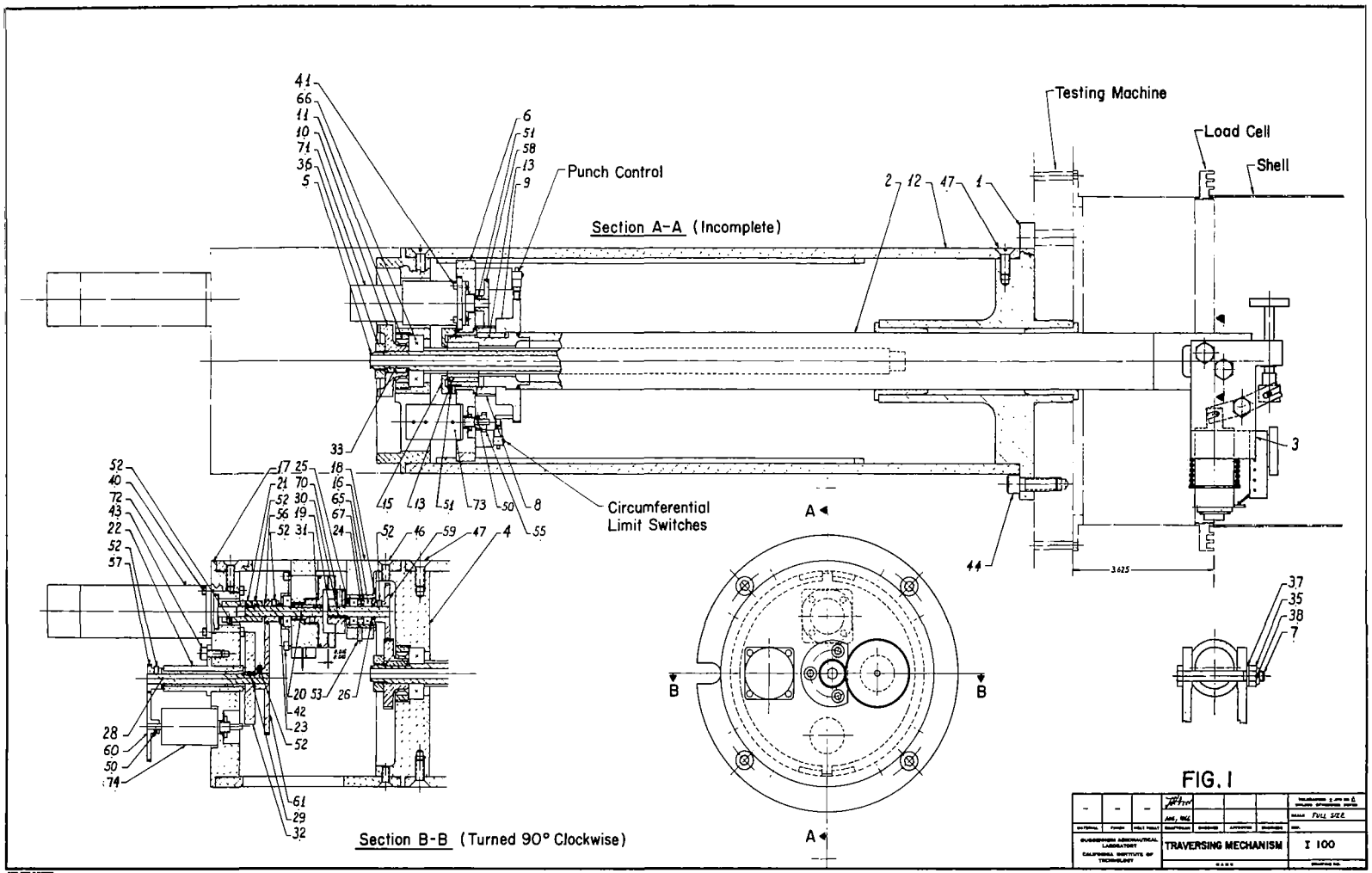
Testing Machine
Load Cell
Shell
Punch Control
Section A-A (Incomplete)
Circumferential
Limit Switches
Section B-B (Turned 90° Clockwise)
TRAVERSING MECHANISM
I 100
FULL SIZE

FIG. I

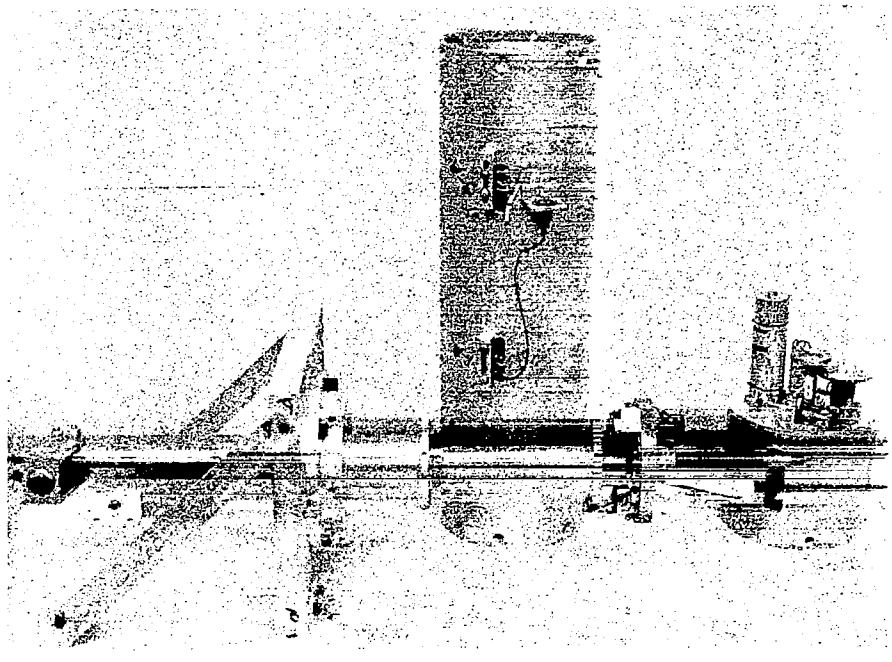

Fig. 2 Scanning Mechanism Unassembled

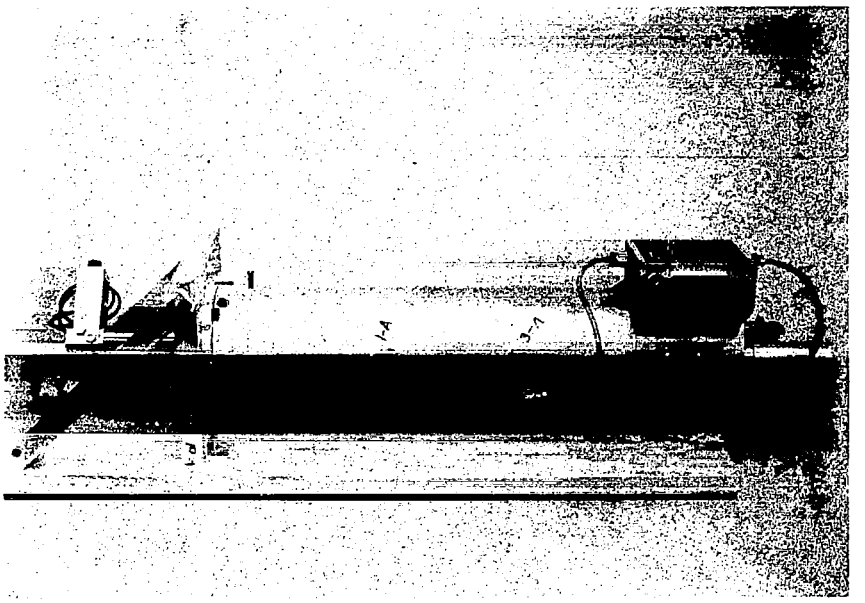

Fig. 3 Scanning Mechanism Assembled

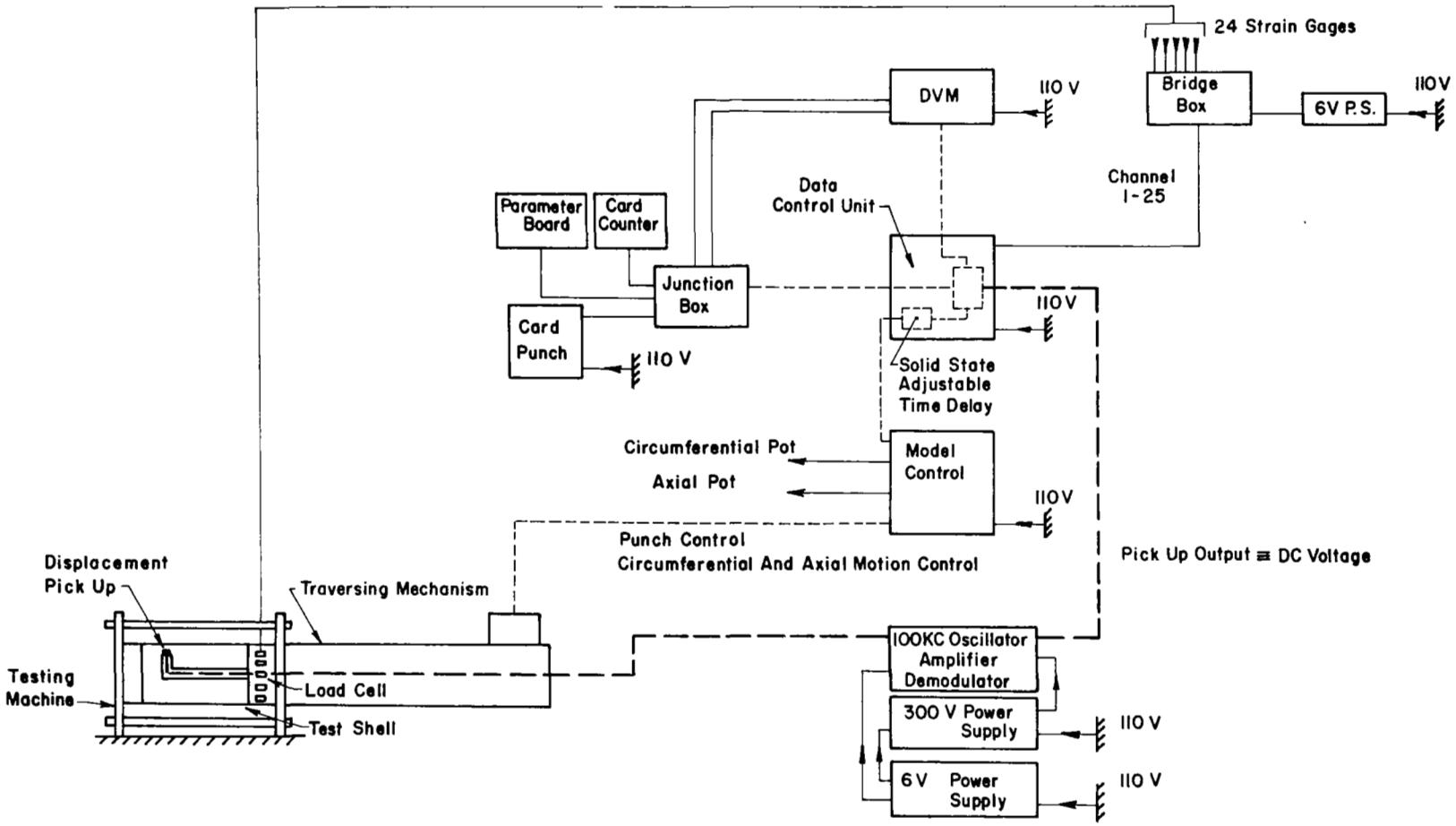

FIG. 4 SCHEMATIC LAYOUT OF THE SHELL BUCKLING EXPERIMENT MEASURING IMPERFECTIONS

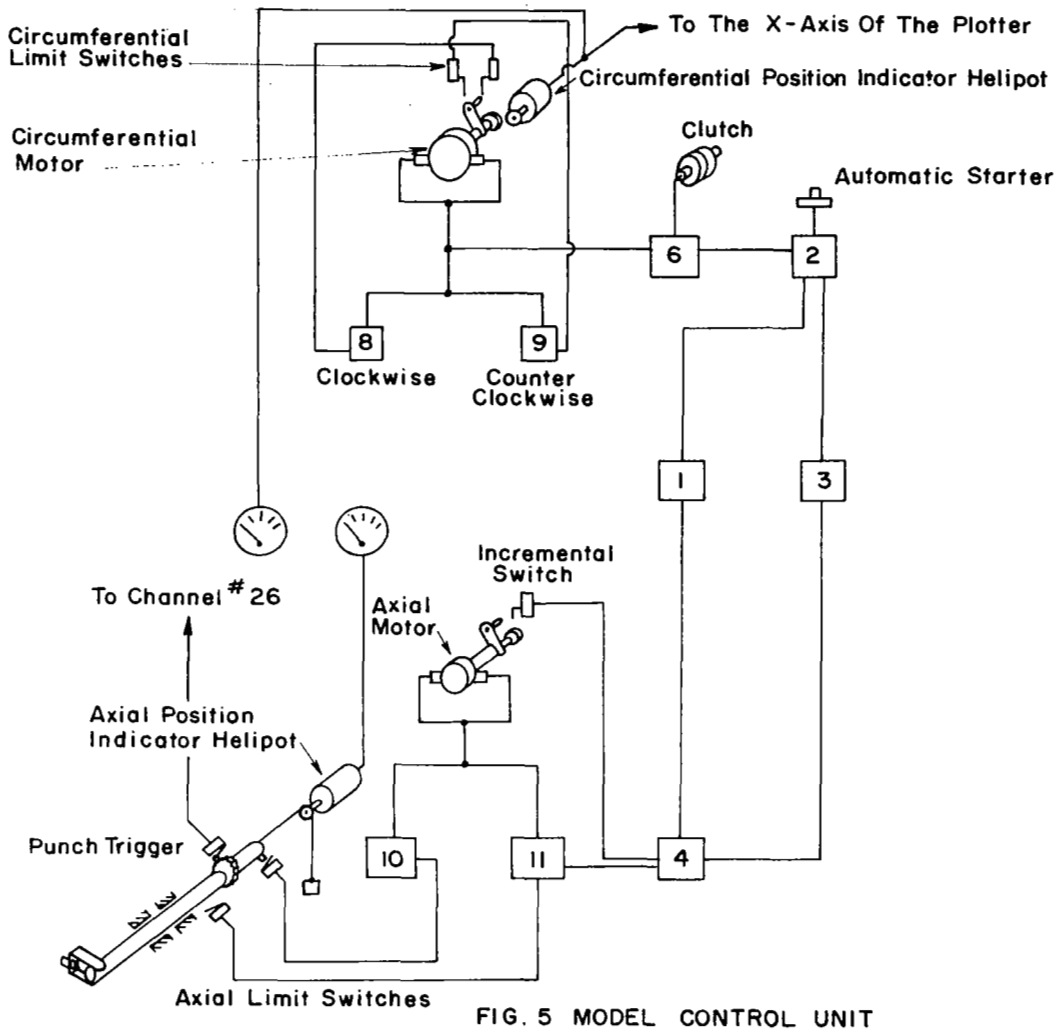

FIG. 5 MODEL CONTROL UNIT

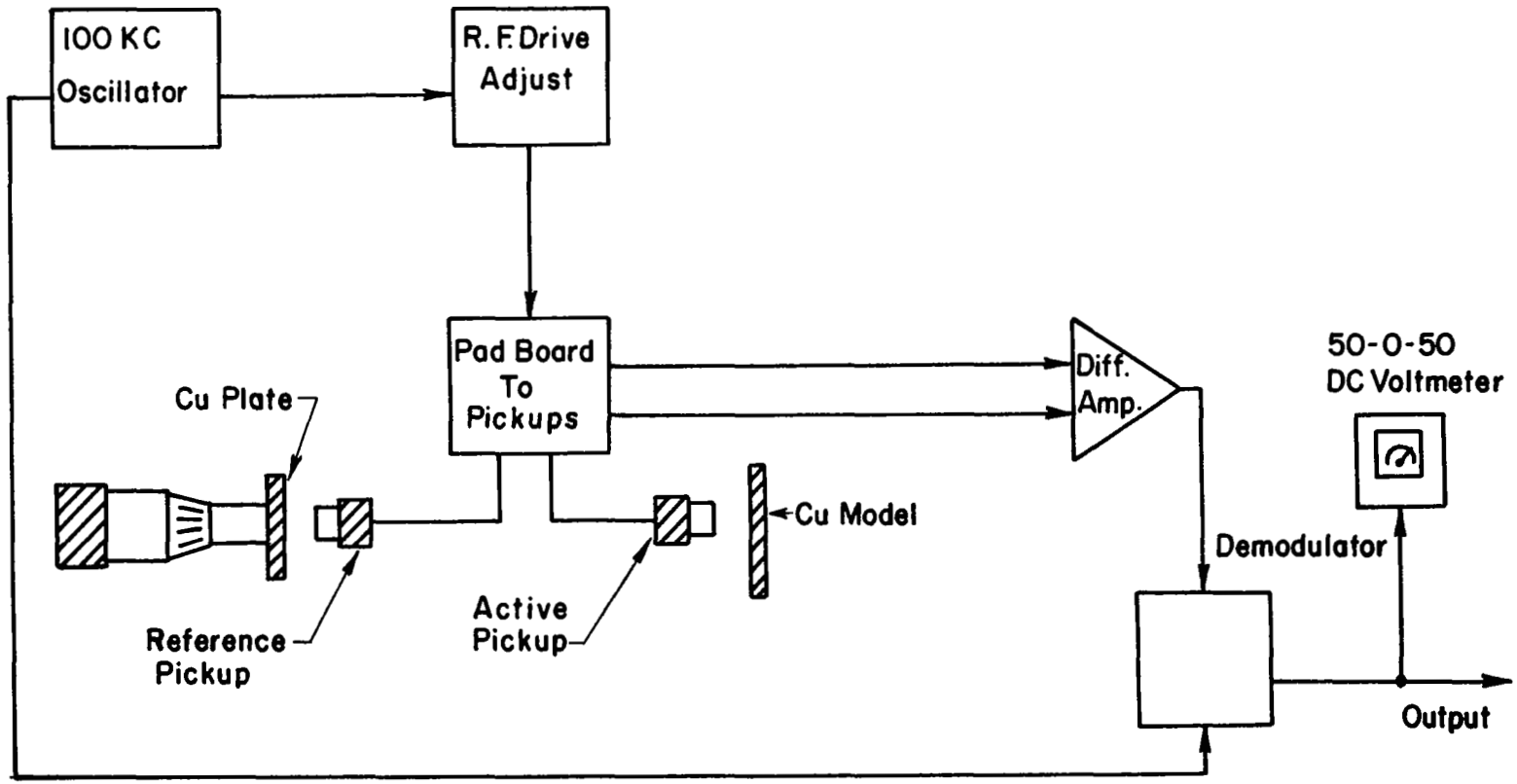

FIG. 6 PICKUP CIRCUIT

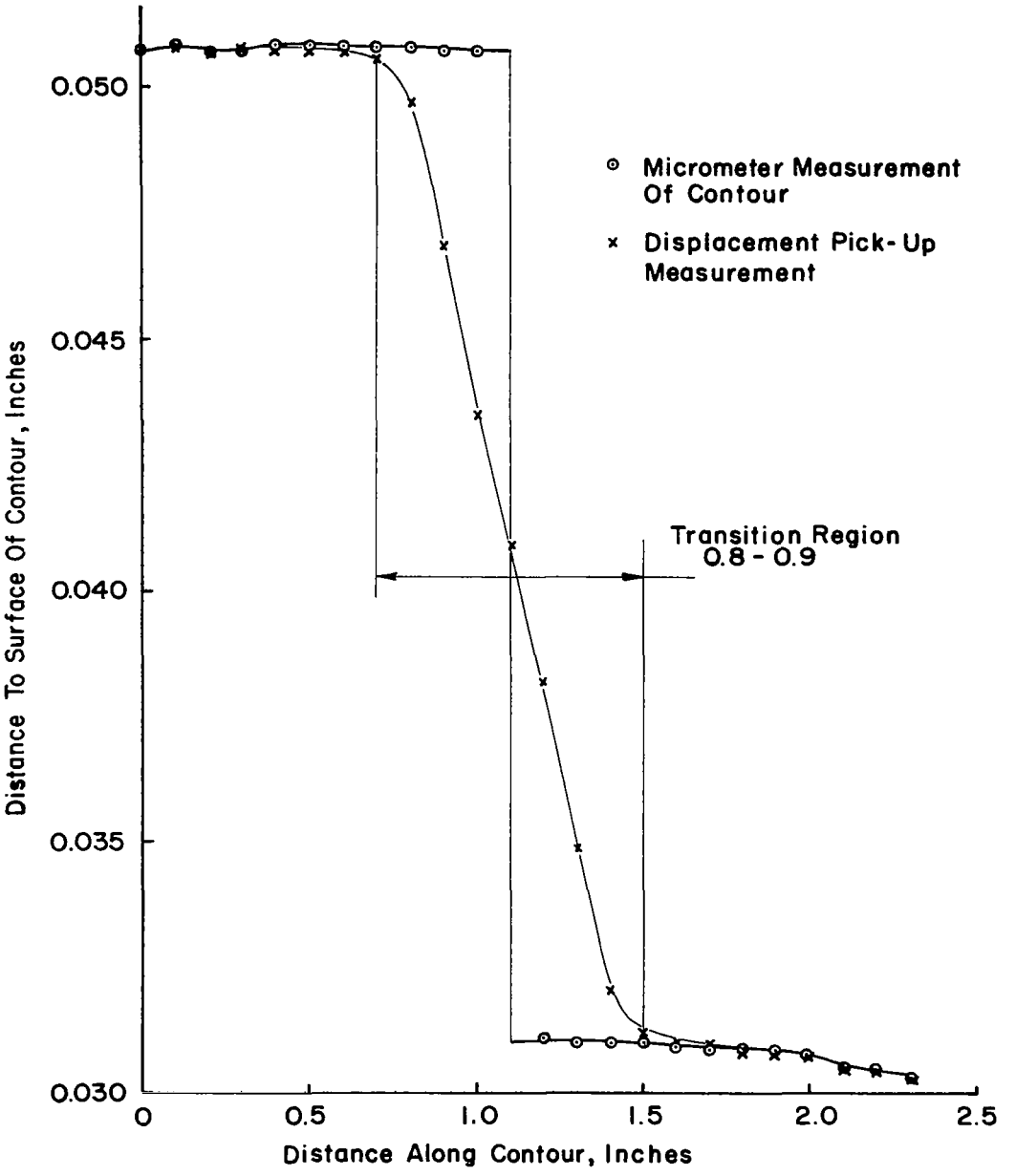

FIG. 7 MICROMETER MEASUREMENT OF KNOWN CONTOUR COMPARED TO PICK-UP MEASUREMENTS

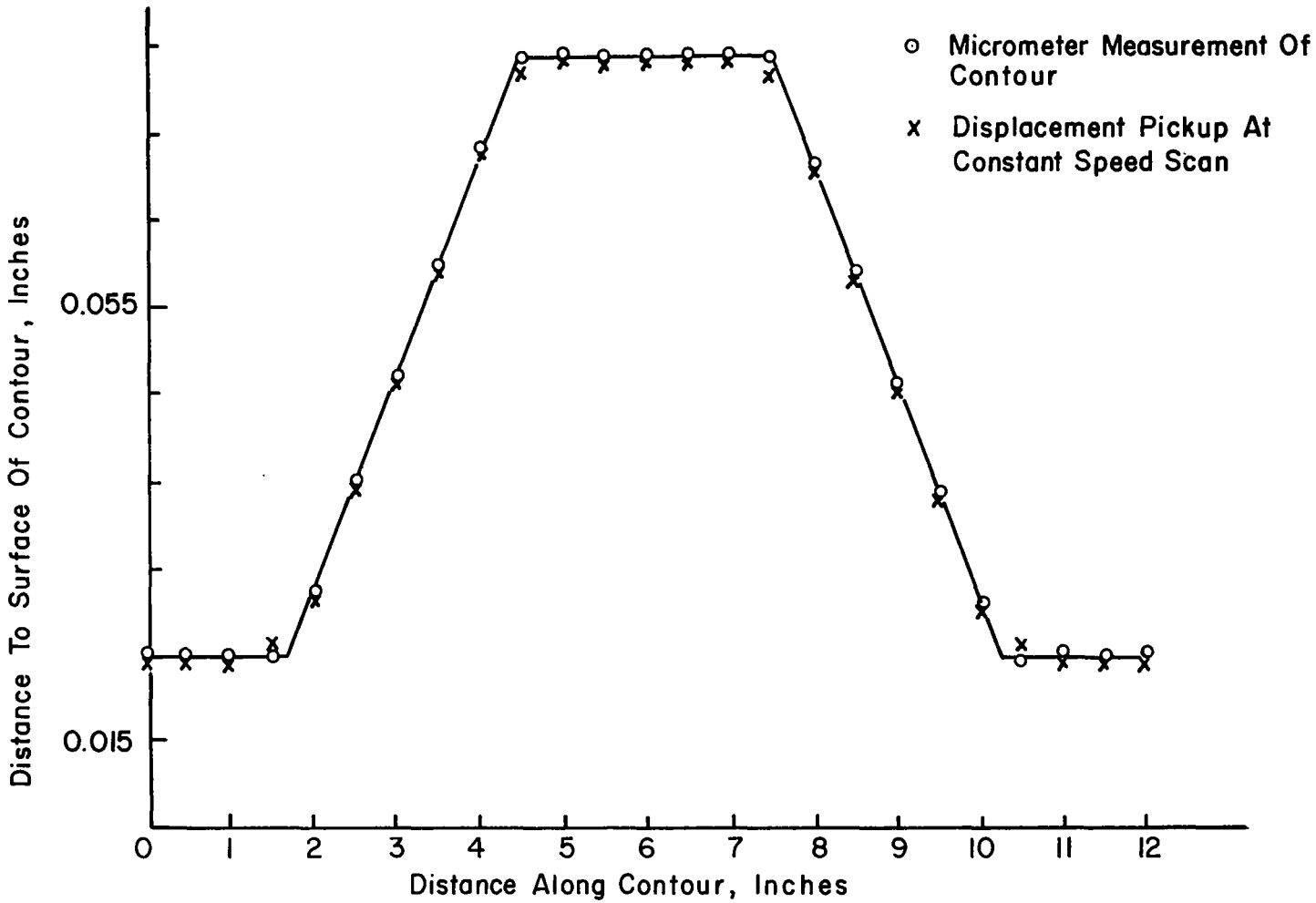

FIG. 8 CONSTANT SPEED TRAVERSE OF KNOWN CONTOUR COMPARED TO "STATIC" MICROMETER MEASUREMENT

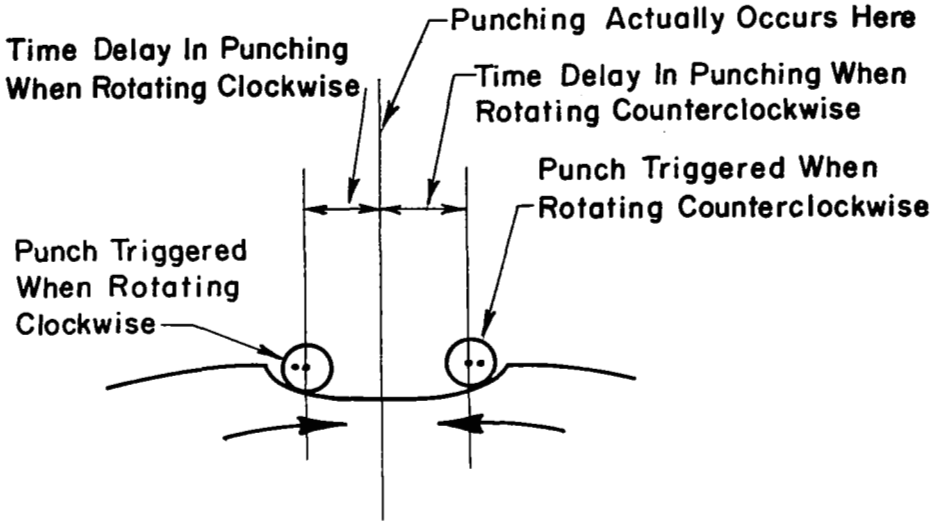

FIG. 9 TIME DELAY FOR PUNCH CONTROL

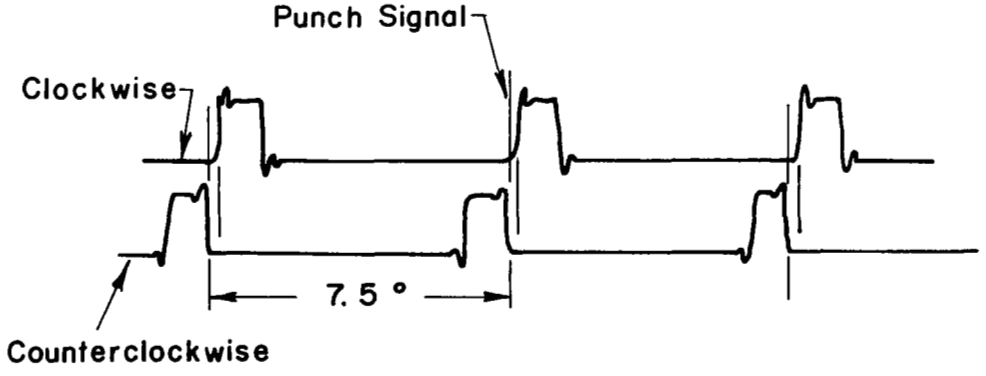

FIG. 10 ADJUSTMENT OF TIME DELAY

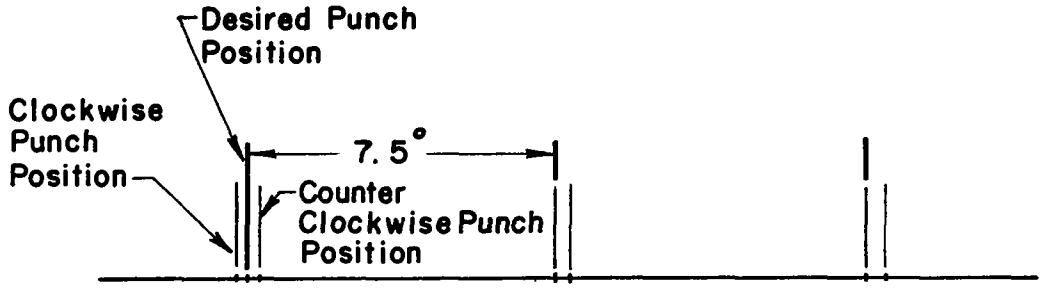

FIG. II MEASURED DEVIATIONS FROM CALCULATED PUNCH POSITION

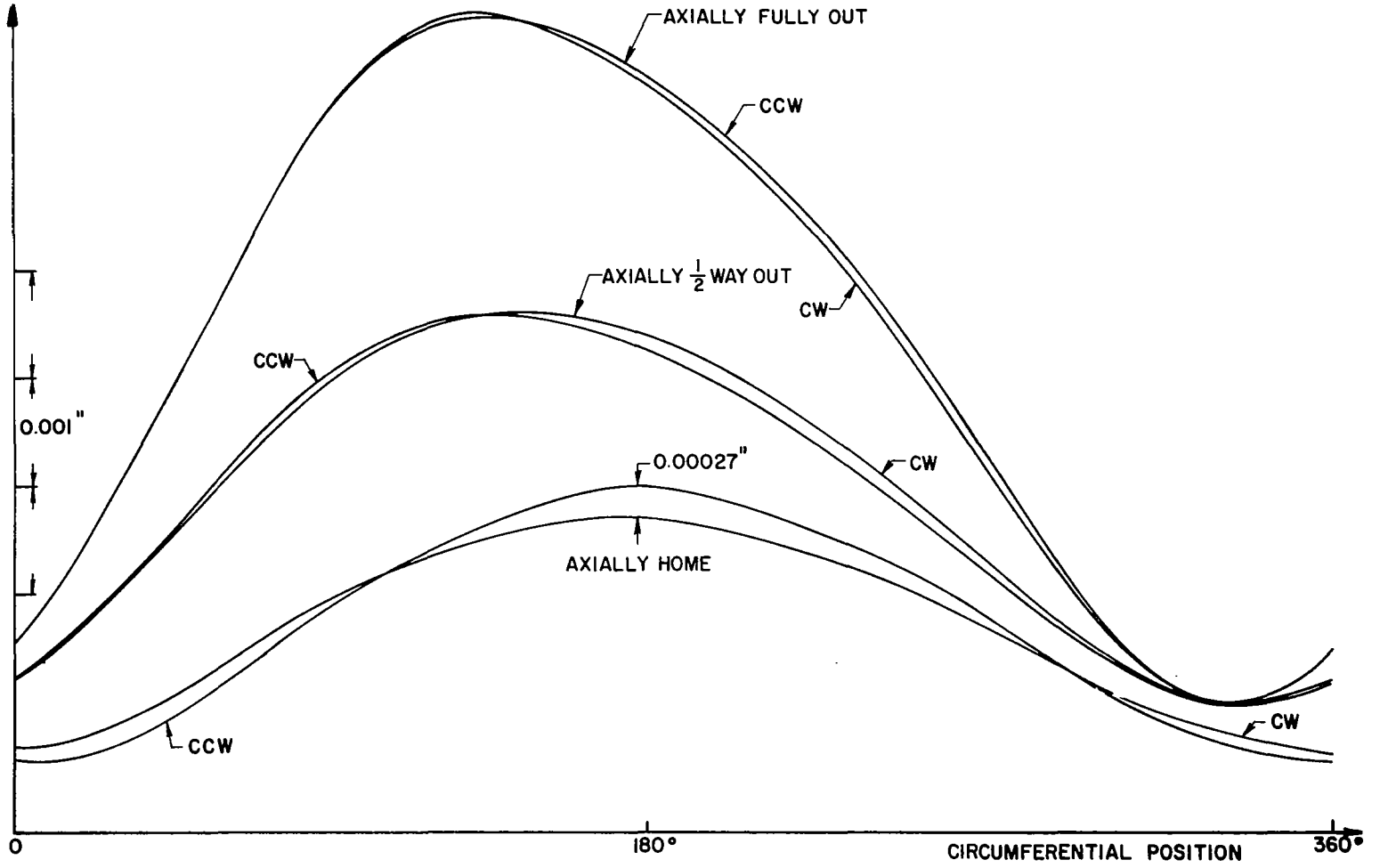

FIG. 12 HYSTERESIS CHECK

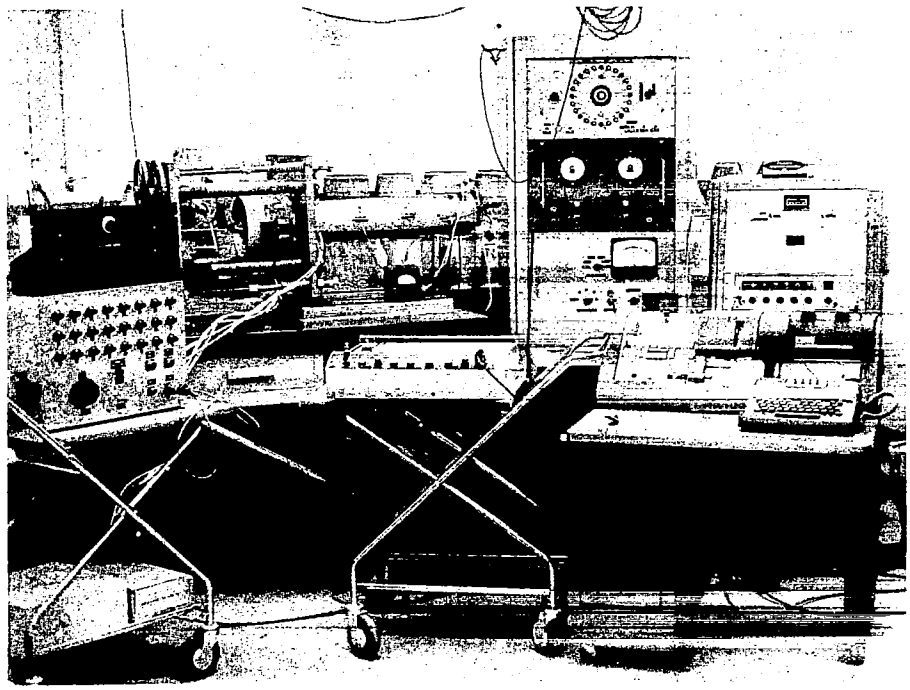

Fig. 13 Testing Machine and Data Acquisition Equipment

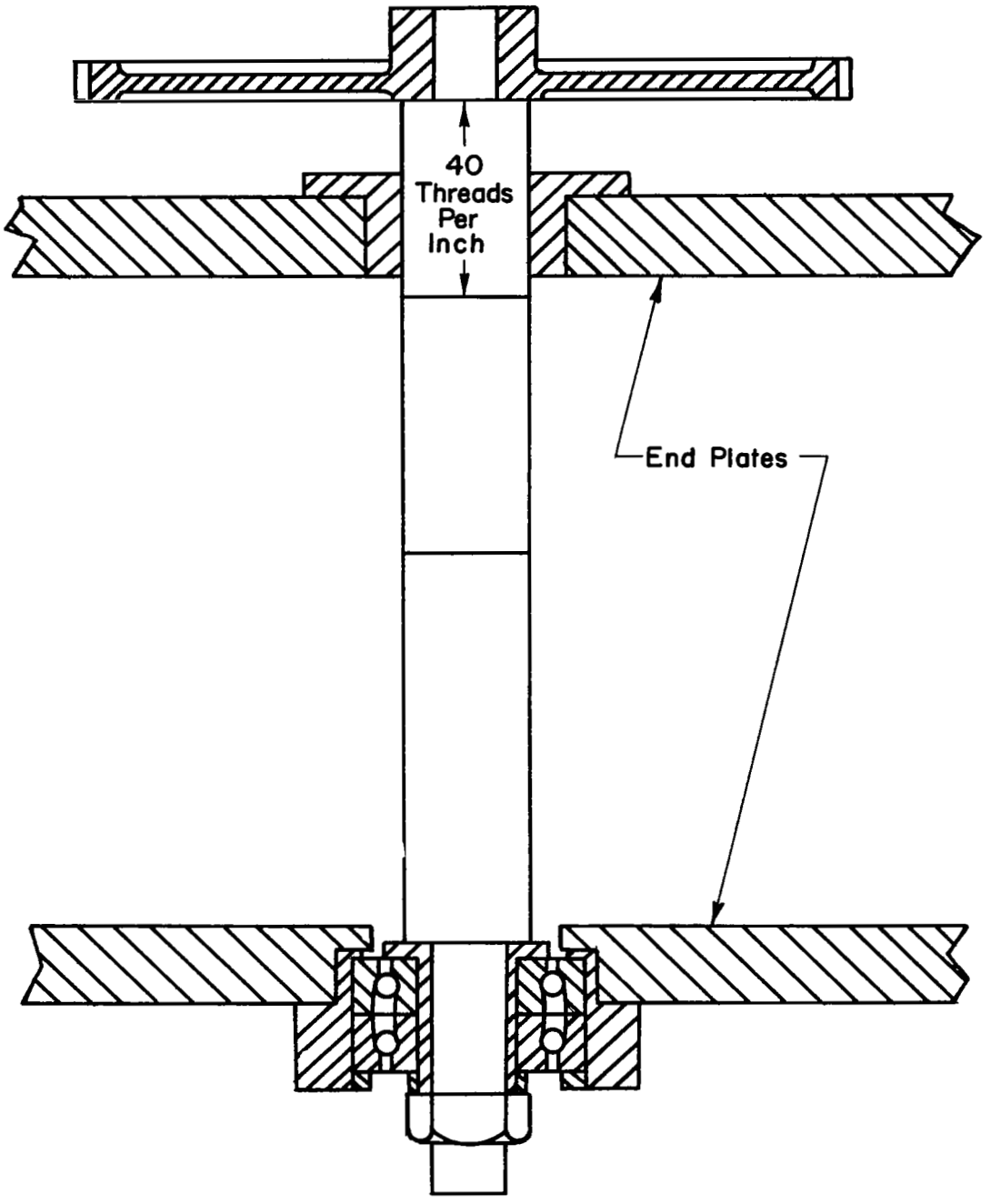

FIG. 14 DETAILS OF TESTING MACHINE LOADING SCREW

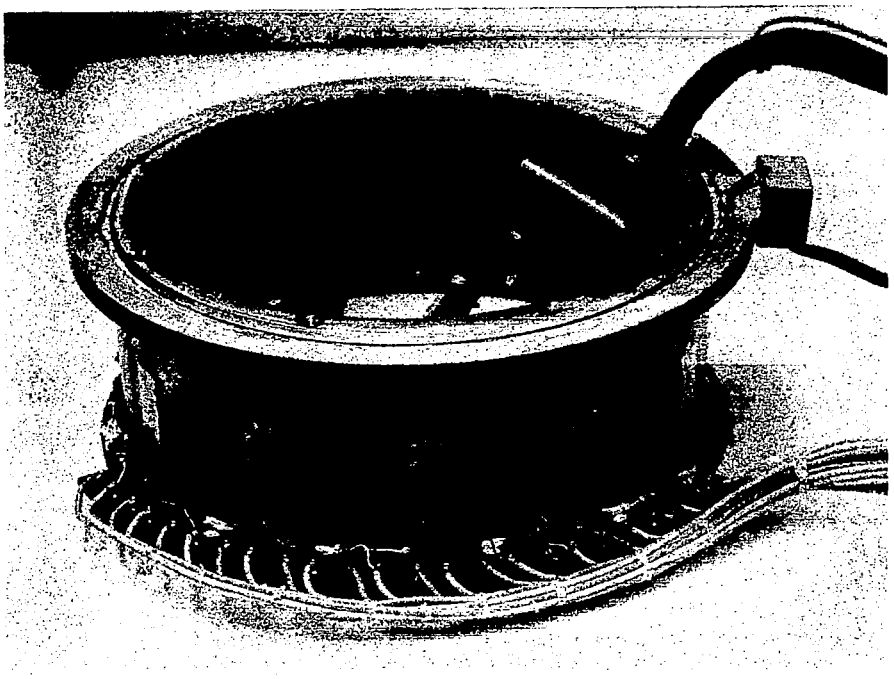

Fig. 15 Load Cell

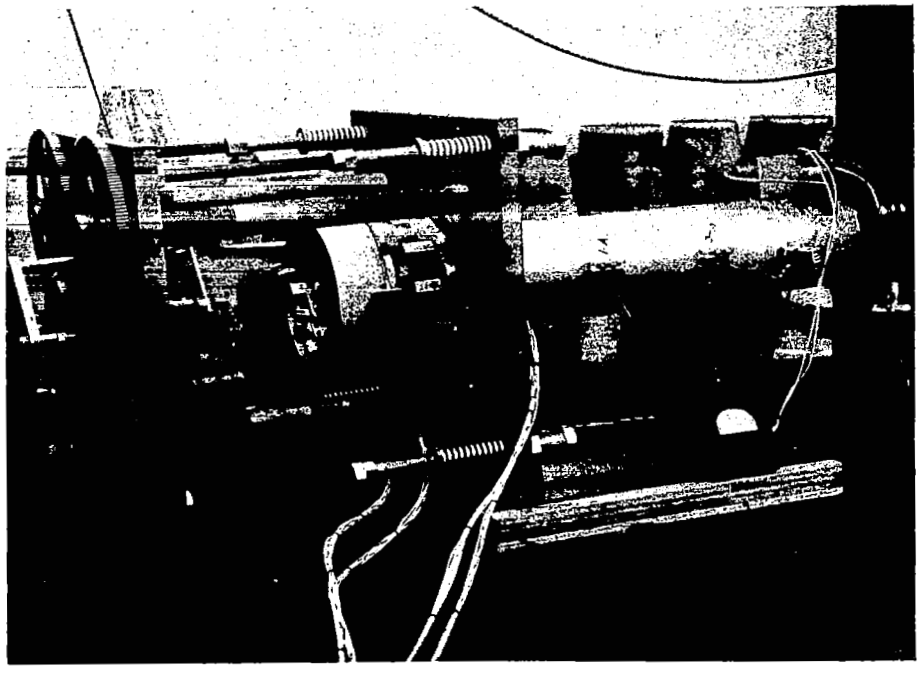

Fig. 16 Pick-up Calibration Set Up

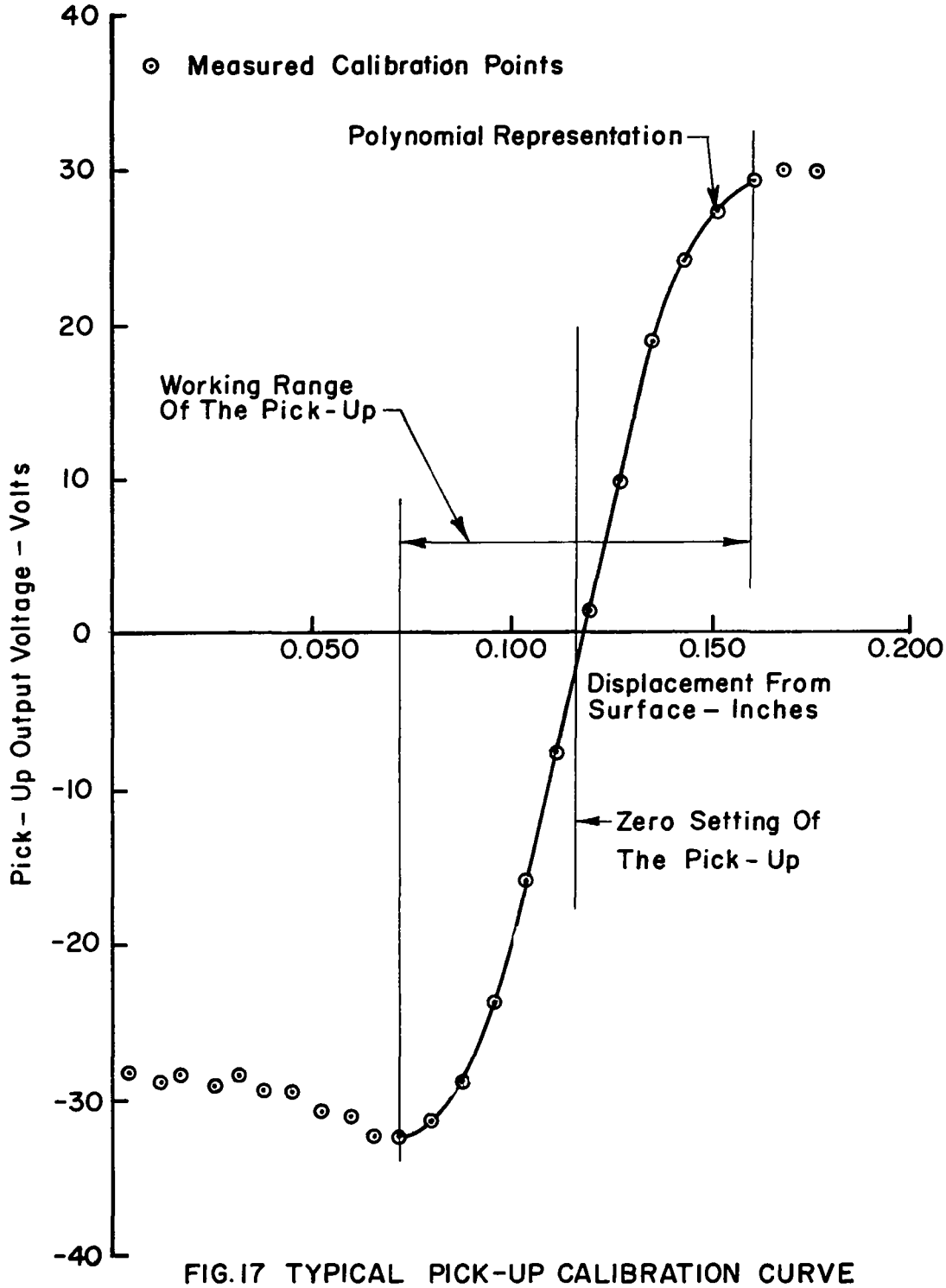

FIG. 17 TYPICAL PICK-UP CALIBRATION CURVE

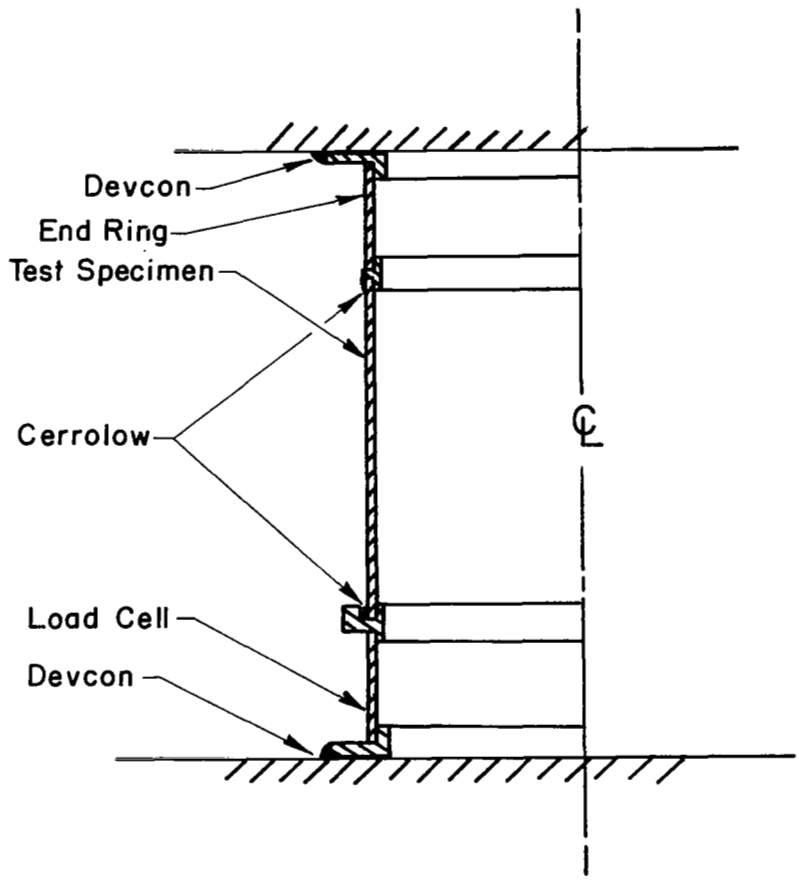

FIG. 18 CYLINDRICAL SHELL TESTING CONFIGURATION

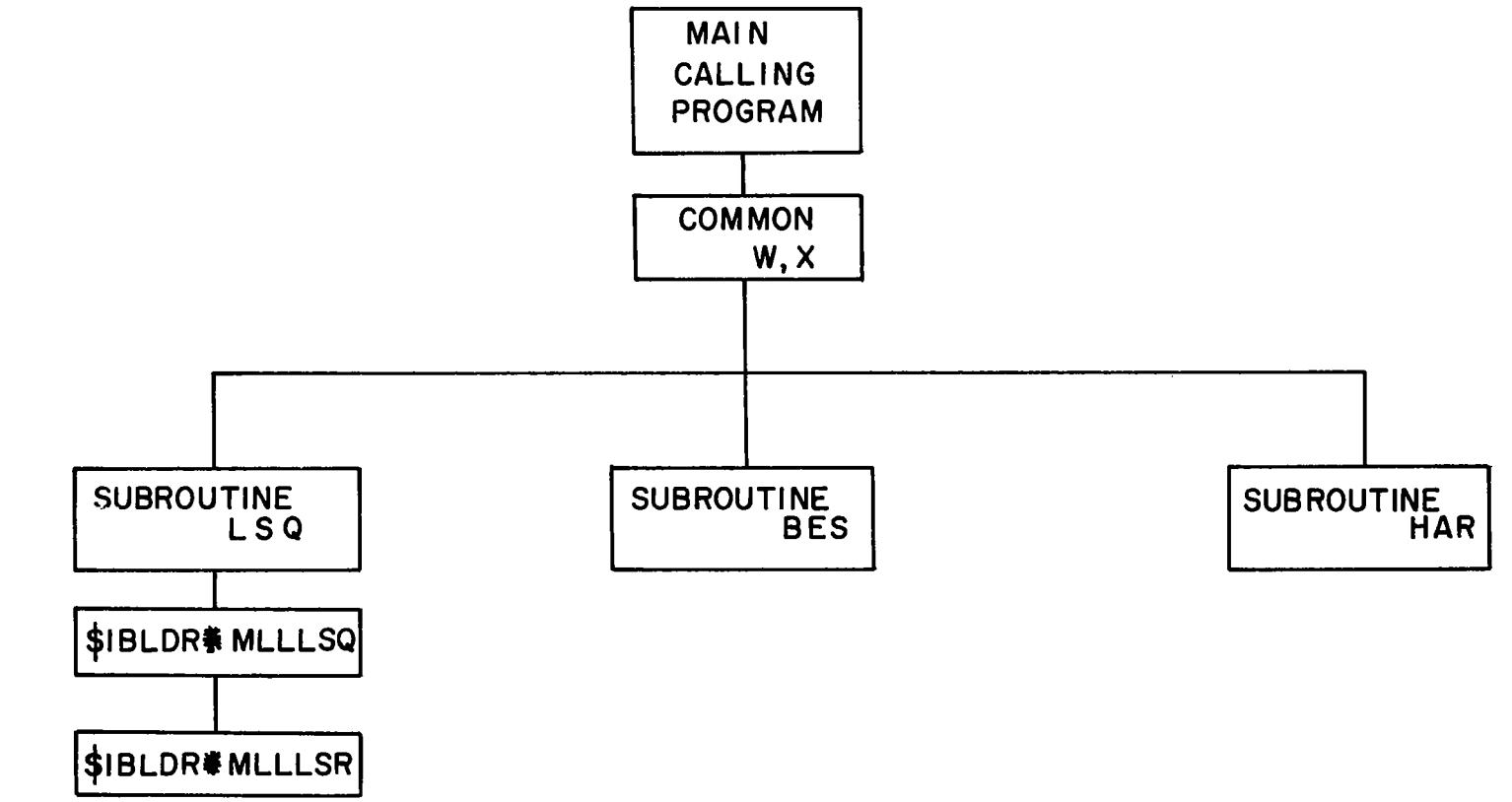

FIG. 19 LAYERED MAIN PROGRAM

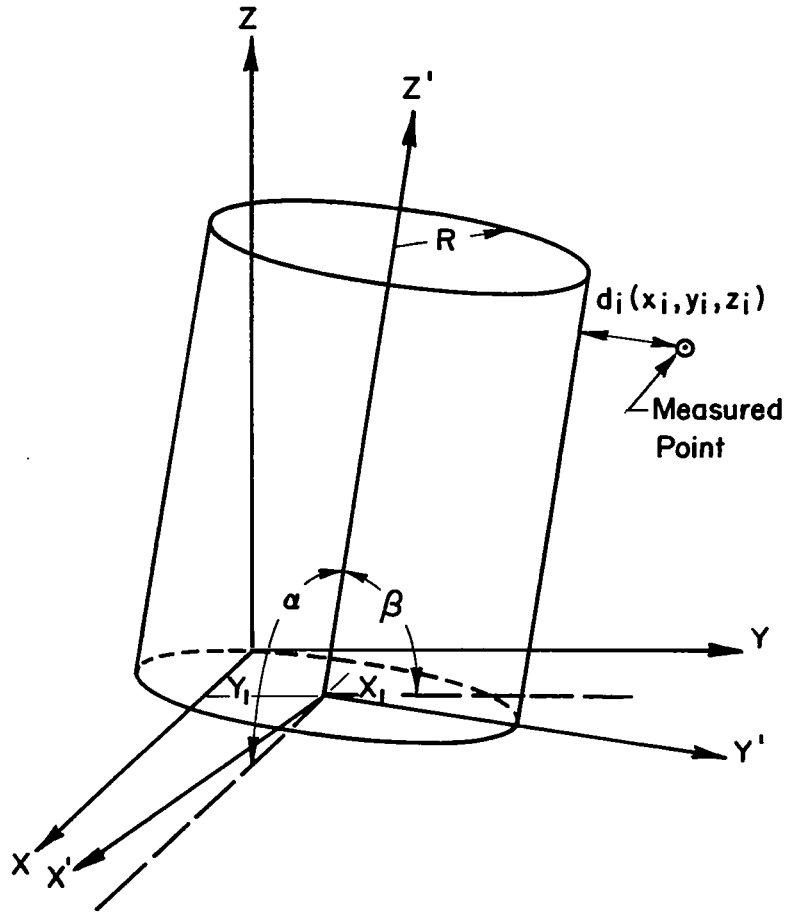

X,Y,Z Reference Axis Of Traversing Pickup
X',Y',Z' Reference Axis Of Best Fit Cylinder
d_i Normal Distance From Measured Point To Best Fit Cylinder

FIG. 20 BEST FIT CYLINDER REFERENCE AXIS

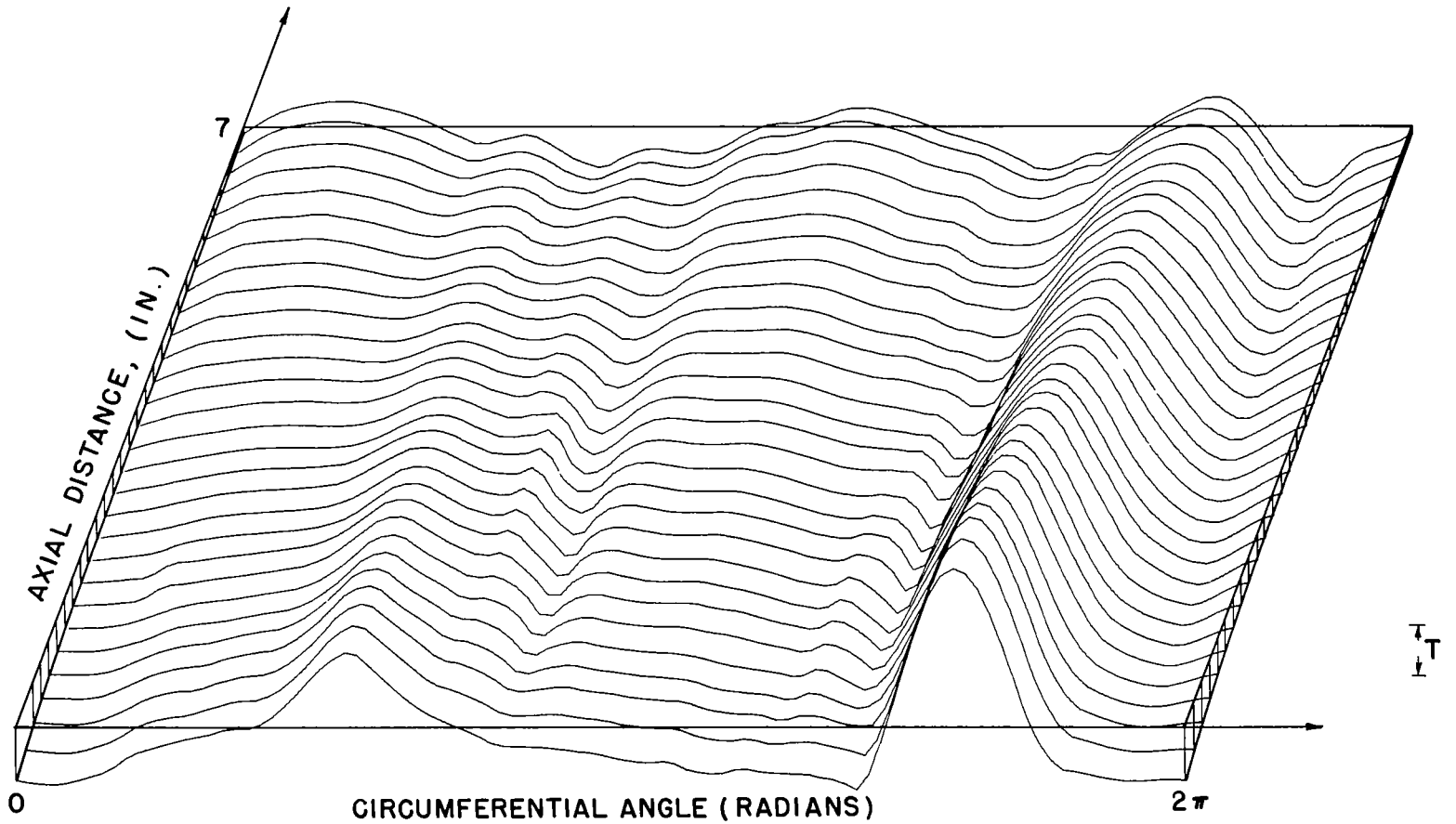

FIG. 21 INITIAL IMPERFECTION, SHELL A-7

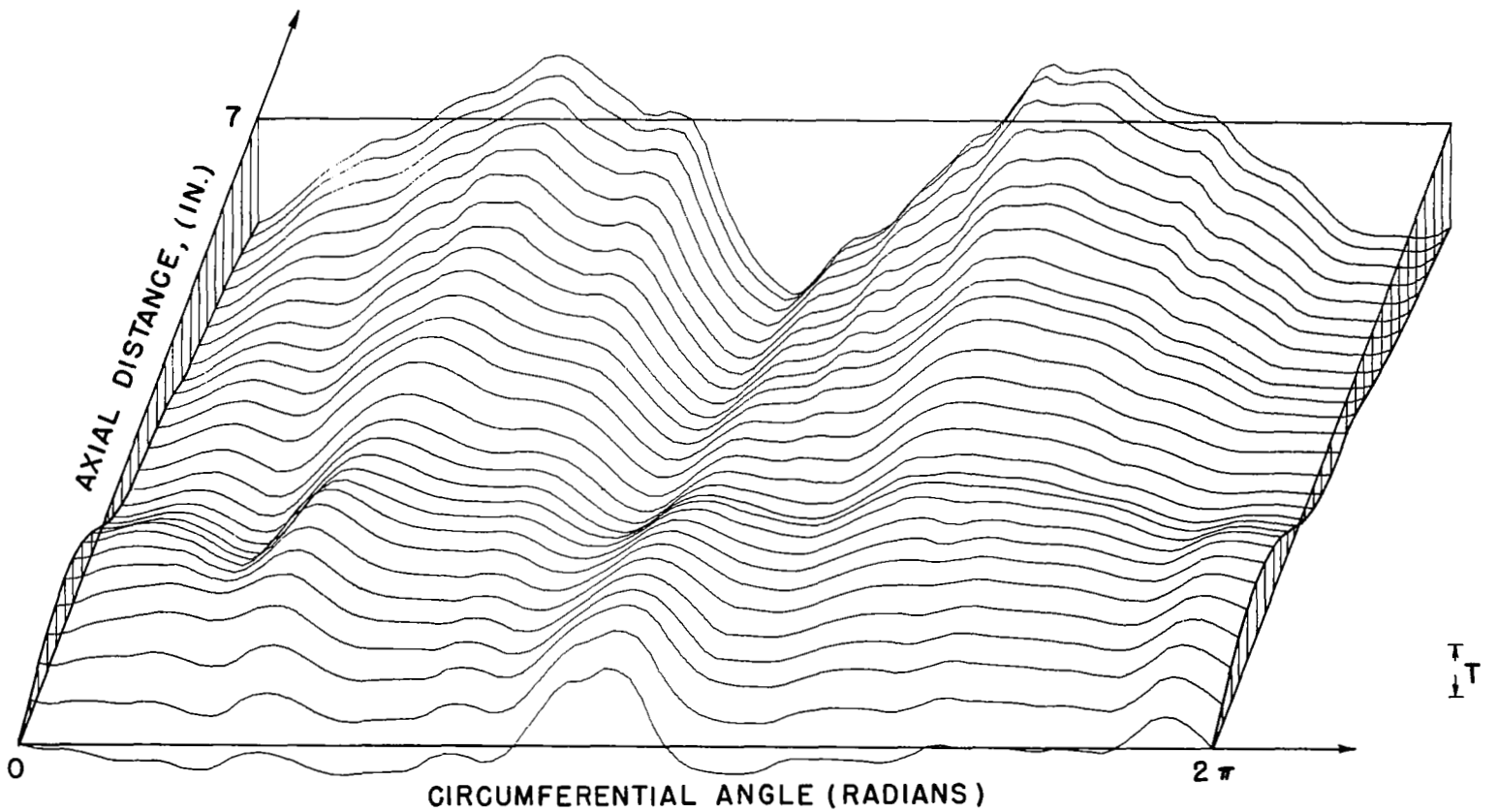

FIG. 22 INITIAL IMPERFECTION, SHELL A-8

FIG. 23 INITIAL IMPERFECTION, SHELL A-9

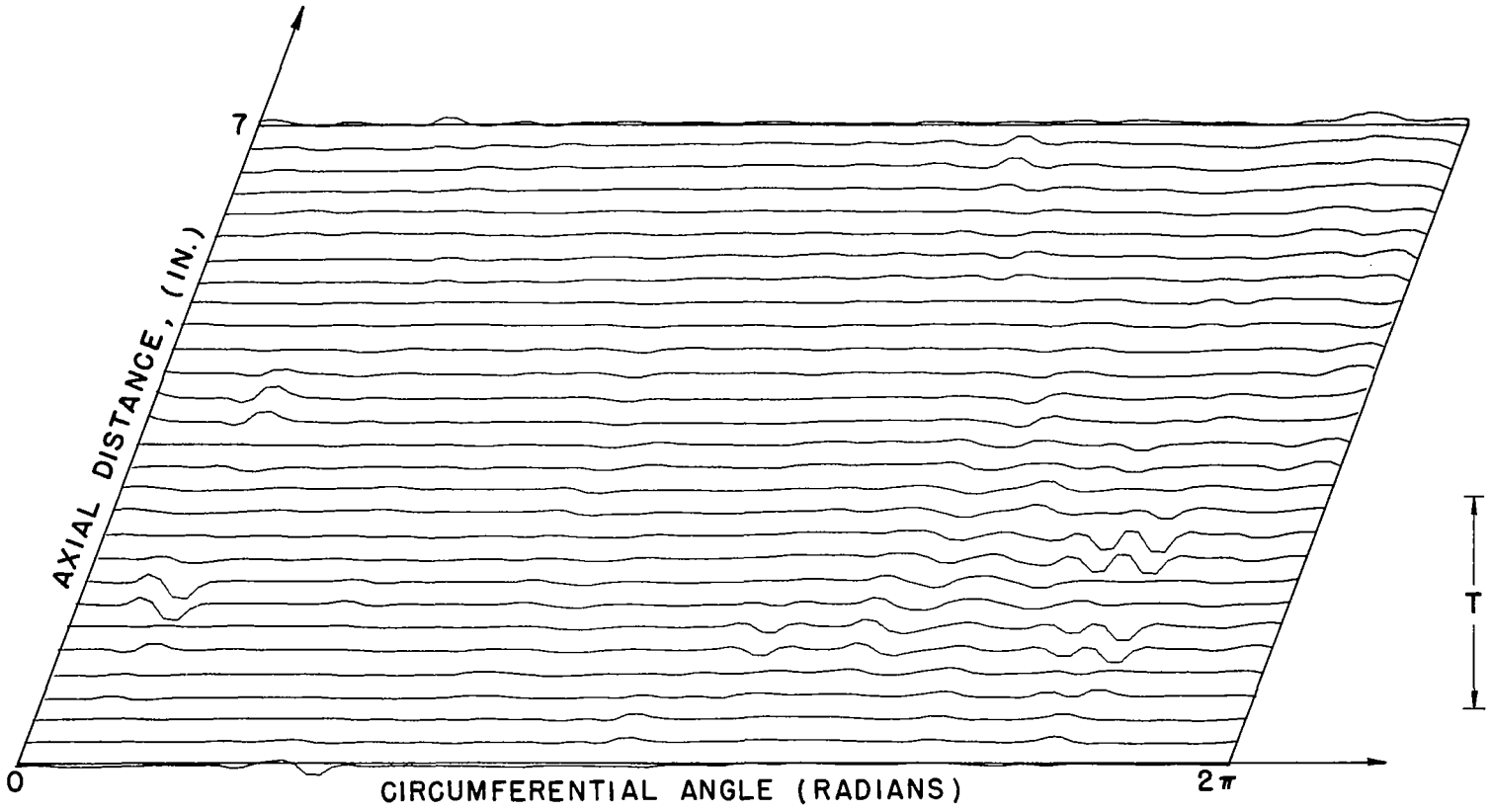

FIG. 24 PREBUCKLING DEFORMATION GROWTH AT $P/P_{CL} = 0.061$, SHELL A-7

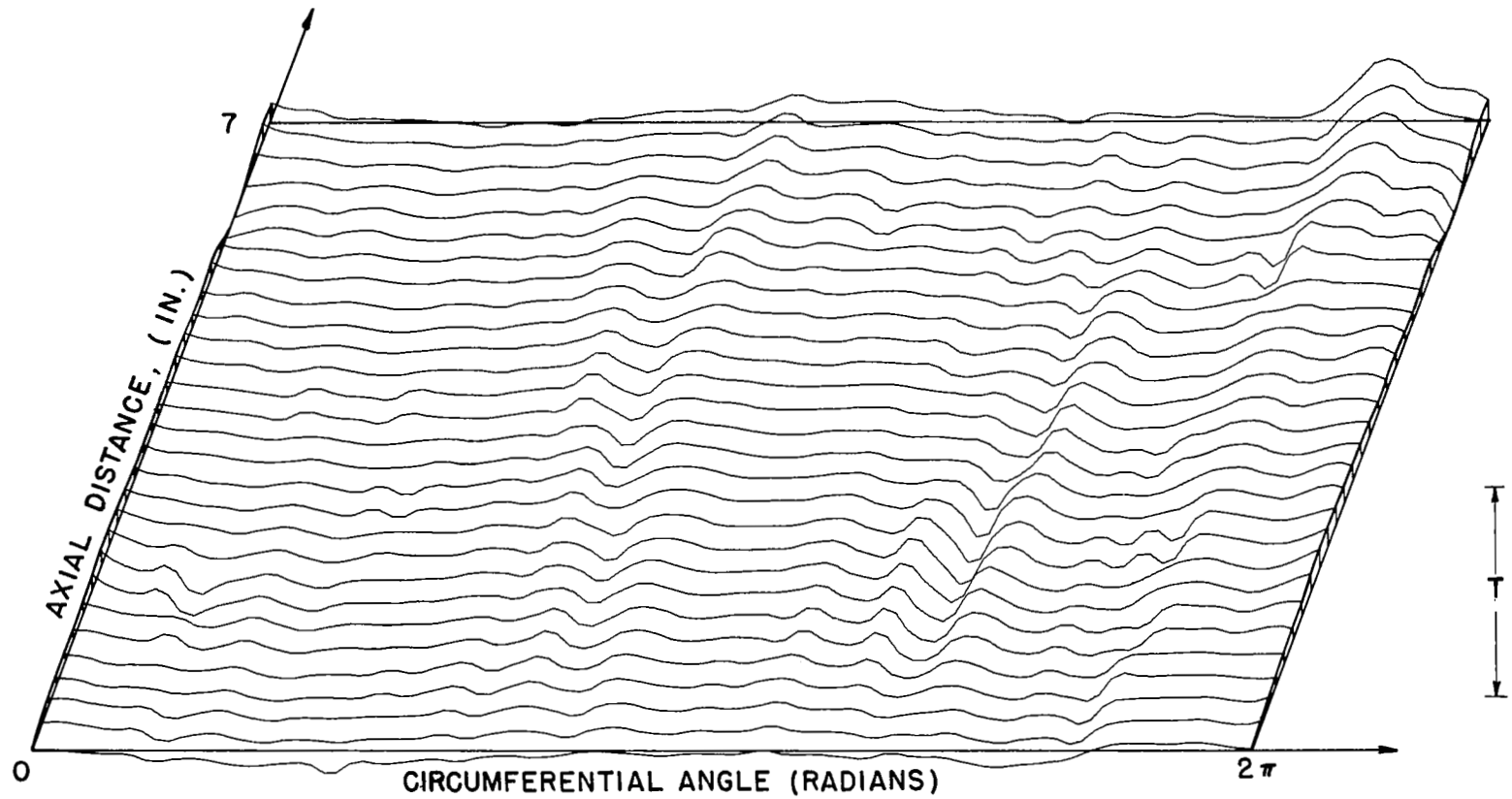

FIG. 25 PREBUCKLING DEFORMATION GROWTH AT P/P_{CL} = 0.325, SHELL A-7

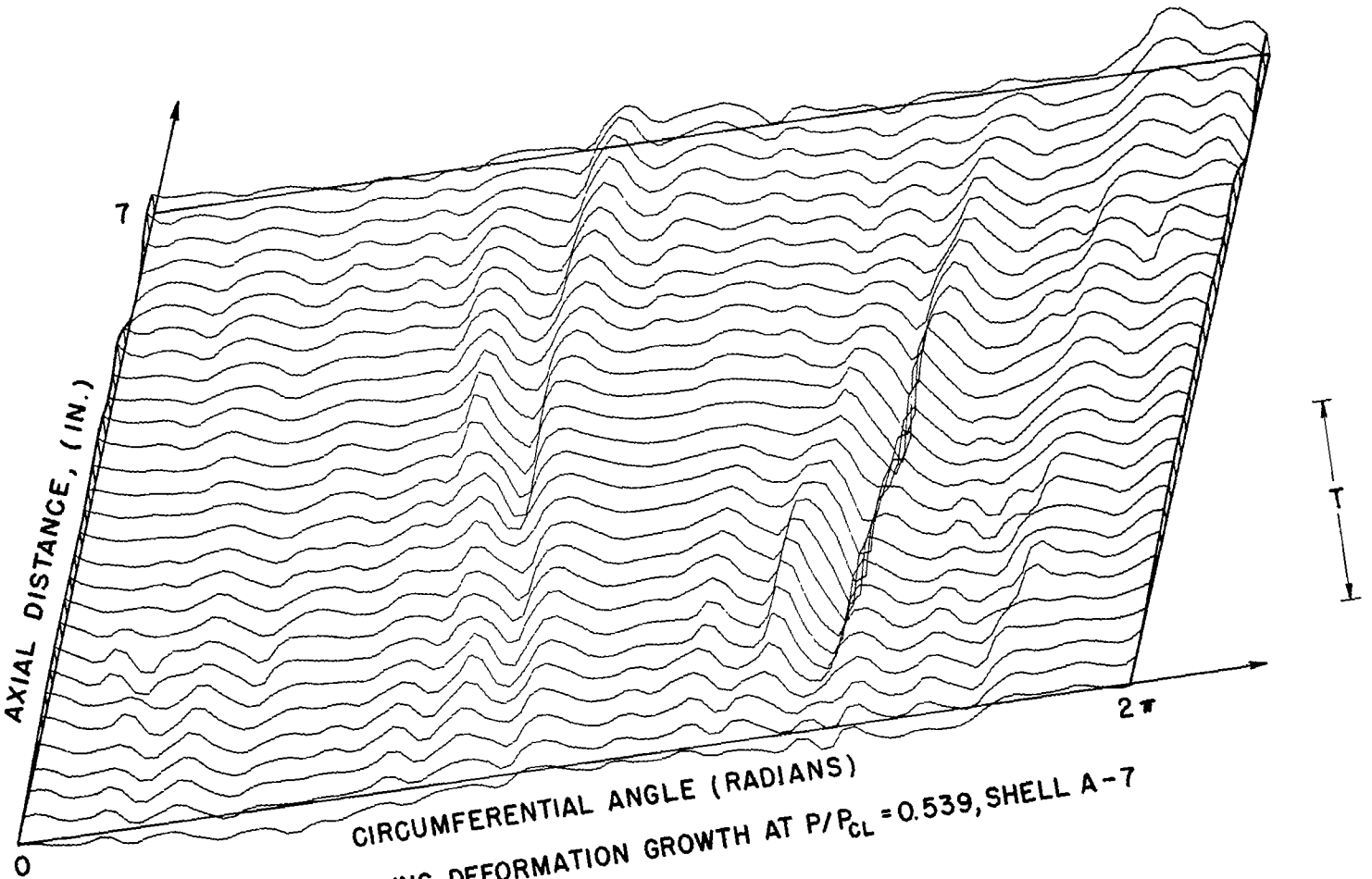

FIG. 26 PREBUCKLING DEFORMATION GROWTH AT $P/P_{CL} = 0.539$, SHELL A-7

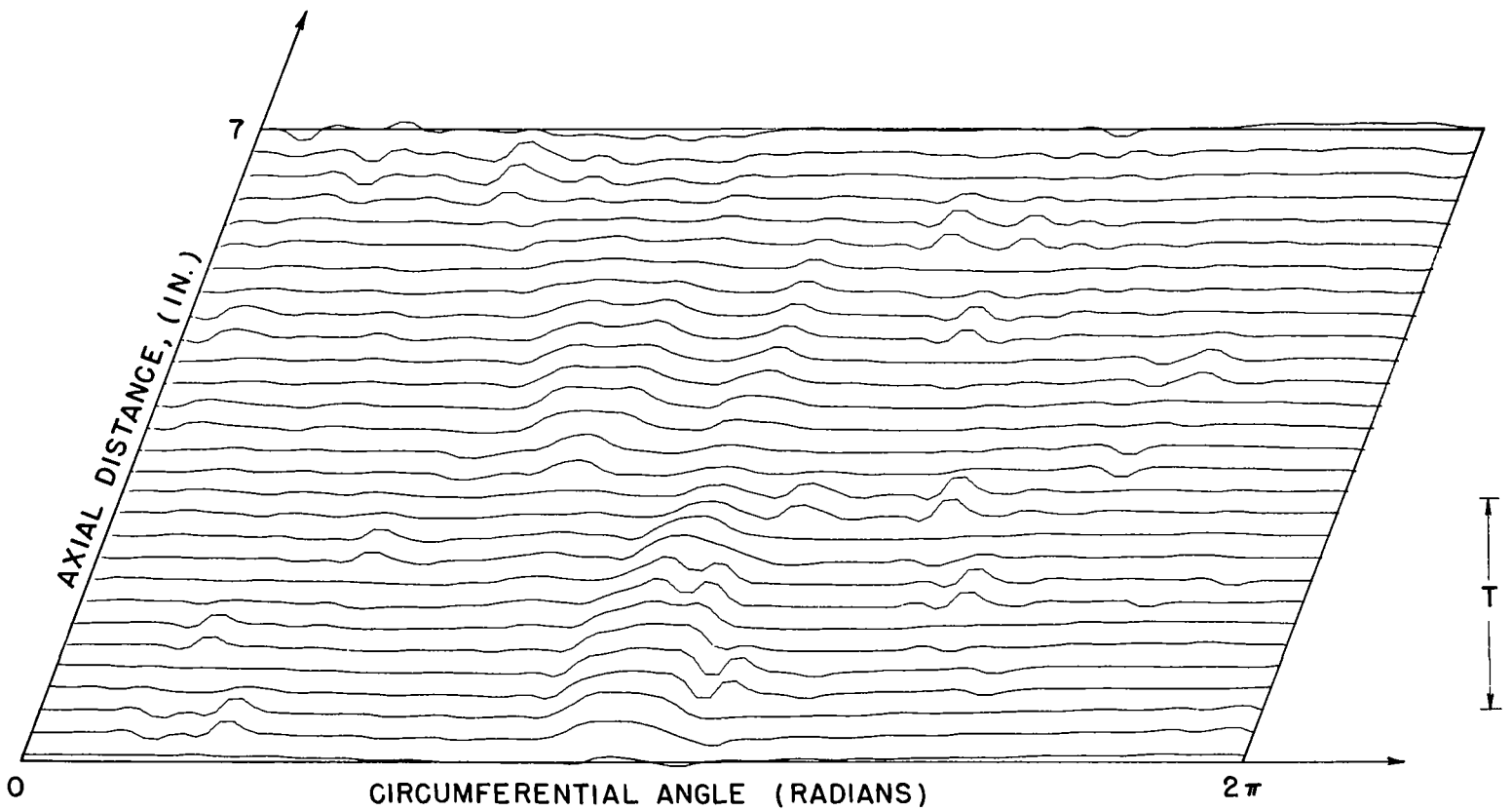

FIG. 27 PREBUCKLING DEFORMATION GROWTH AT $P/P_{CL} = 0.047$, SHELL A-8

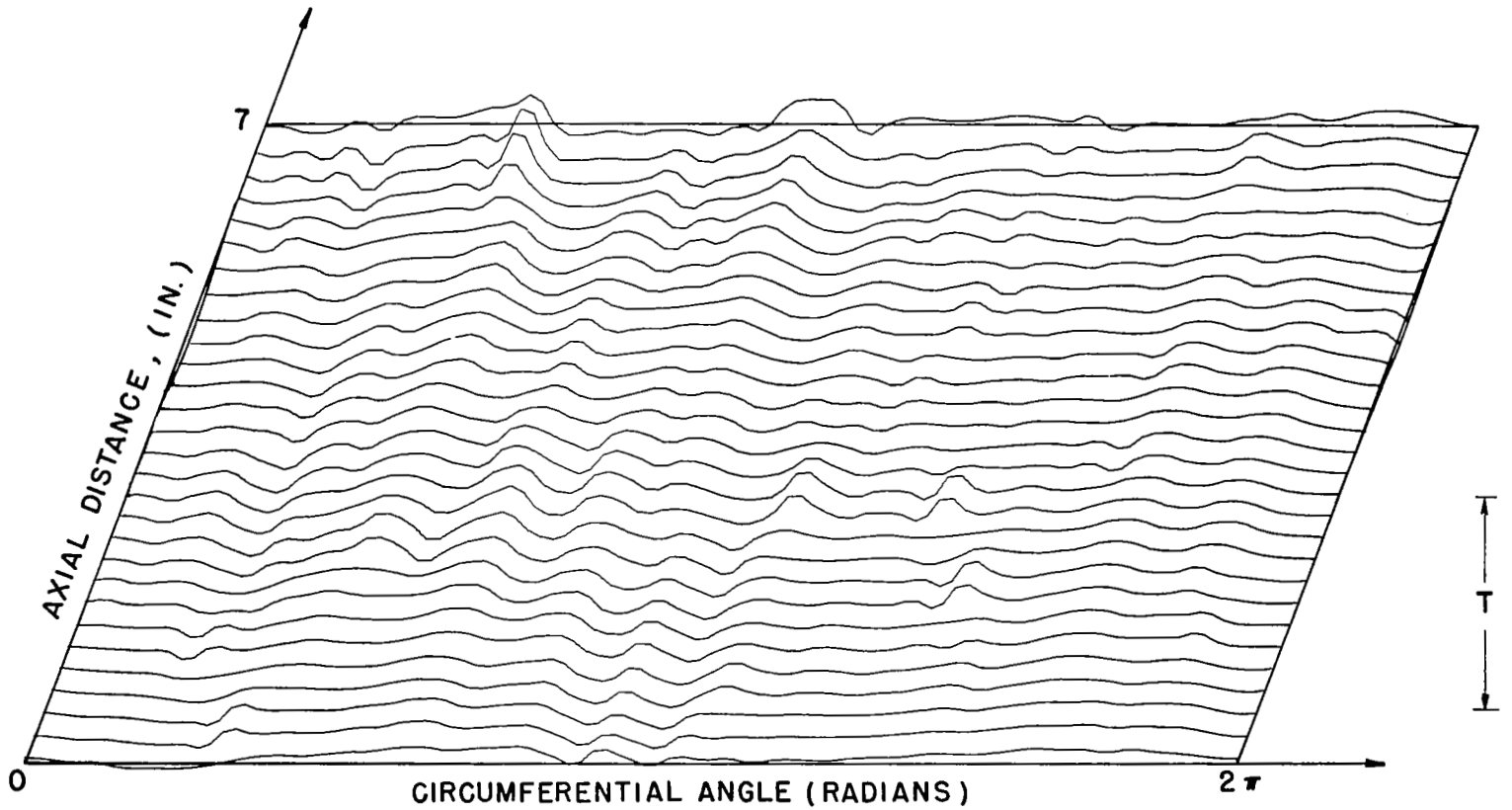

FIG. 28 PREBUCKLING DEFORMATION GROWTH AT P/P_{CL} = 0.339, SHELL A-8

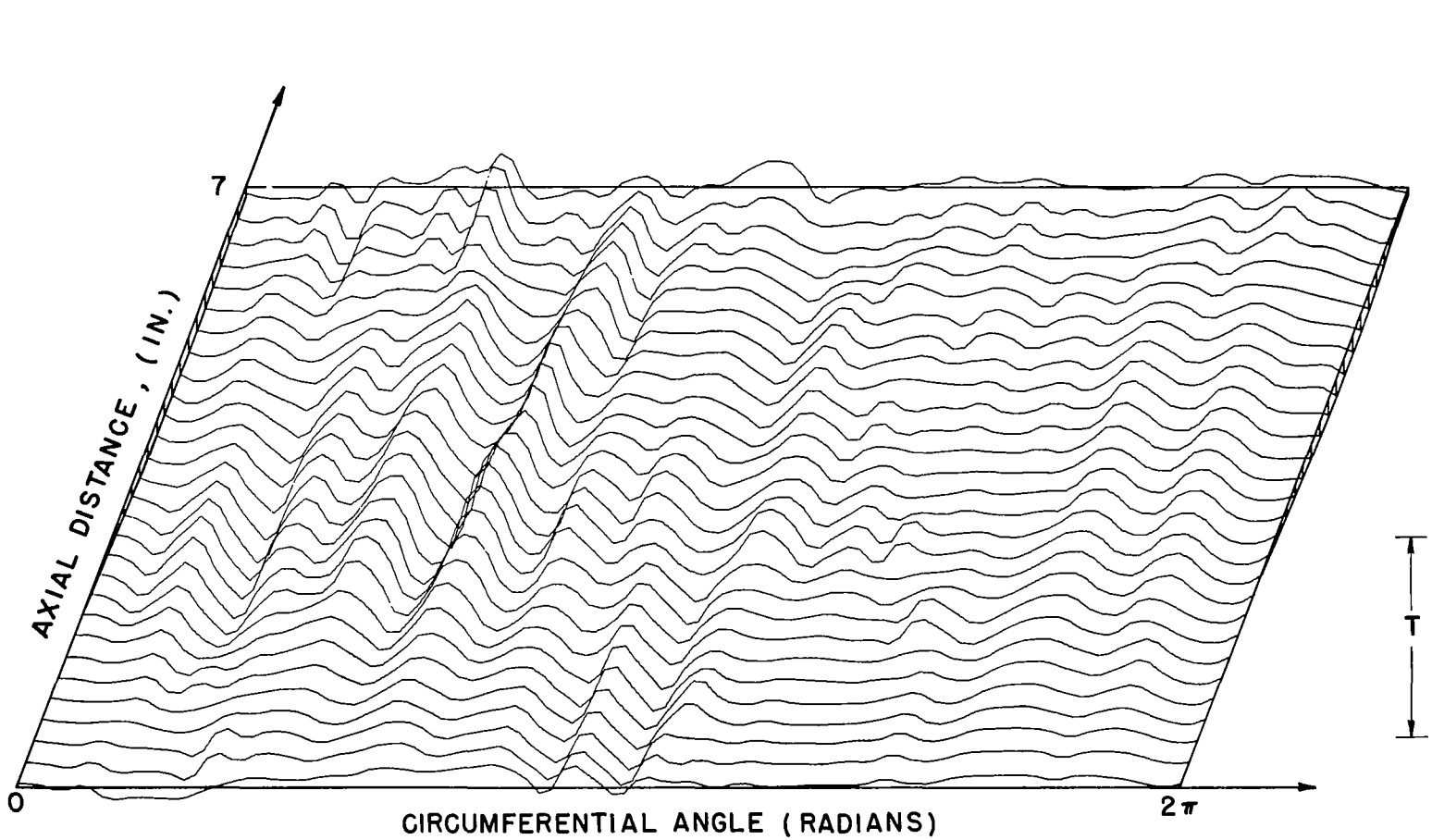

FIG. 29 PREBUCKLING DEFORMATION GROWTH AT $P/P_{CL} = 0.637$, SHELL A-8

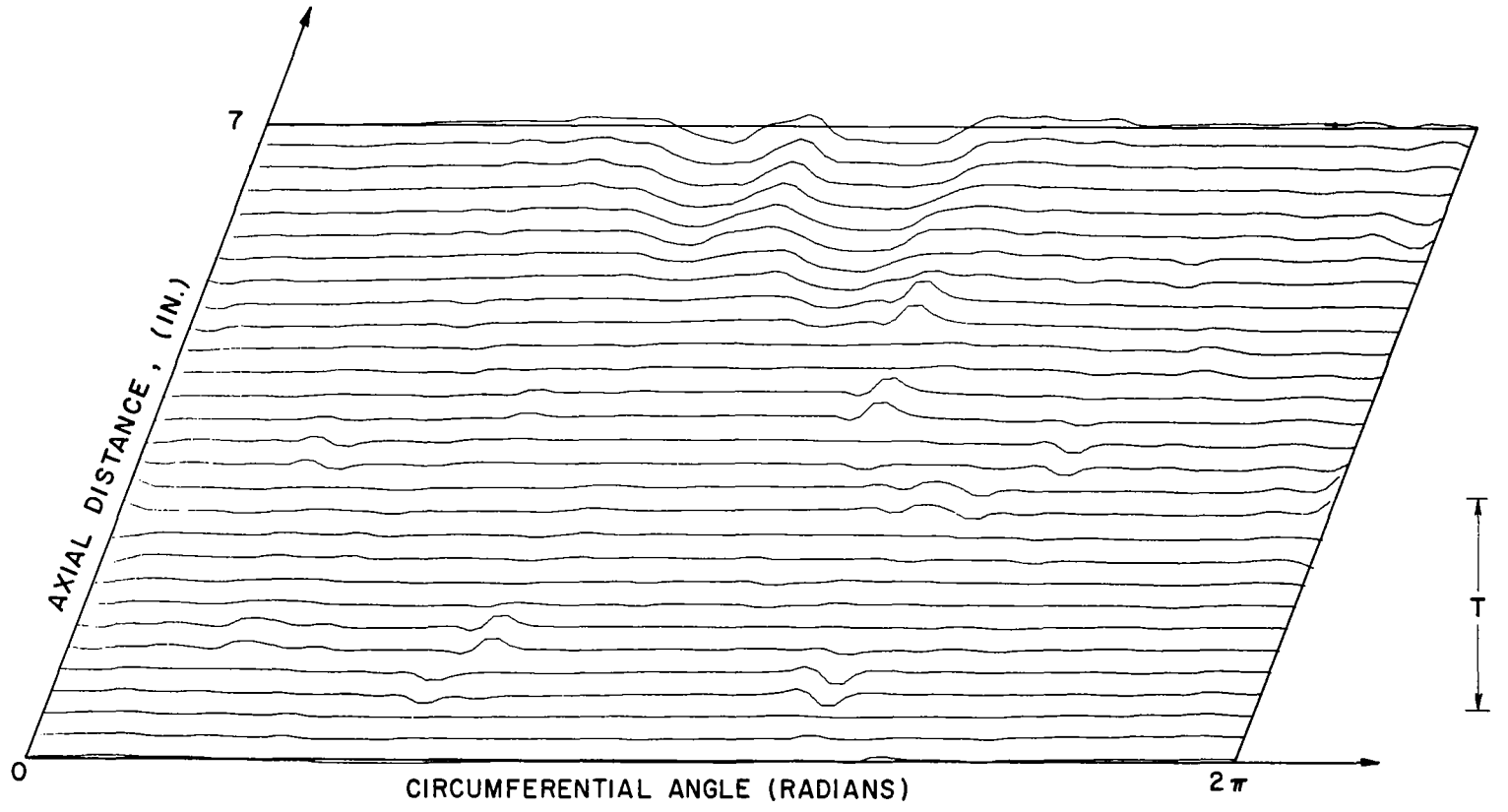

FIG. 30 PREBUCKLING DEFORMATION GROWTH AT $P/P_{CL} = 0.042$, SHELL A-9

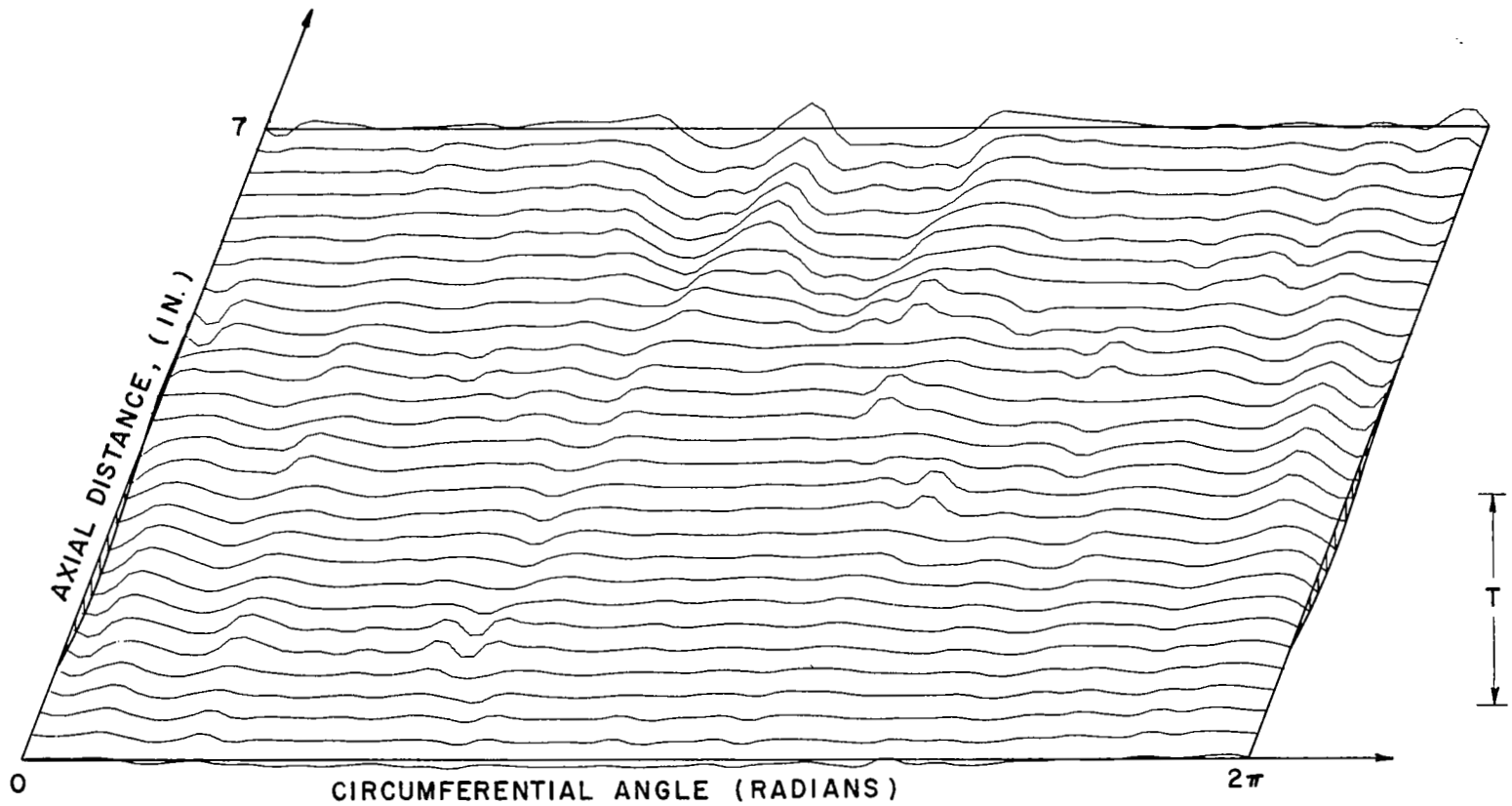

FIG. 31 PREBUCKLING DEFORMATION GROWTH AT P/P_{CL} = 0.360, SHELL A-9

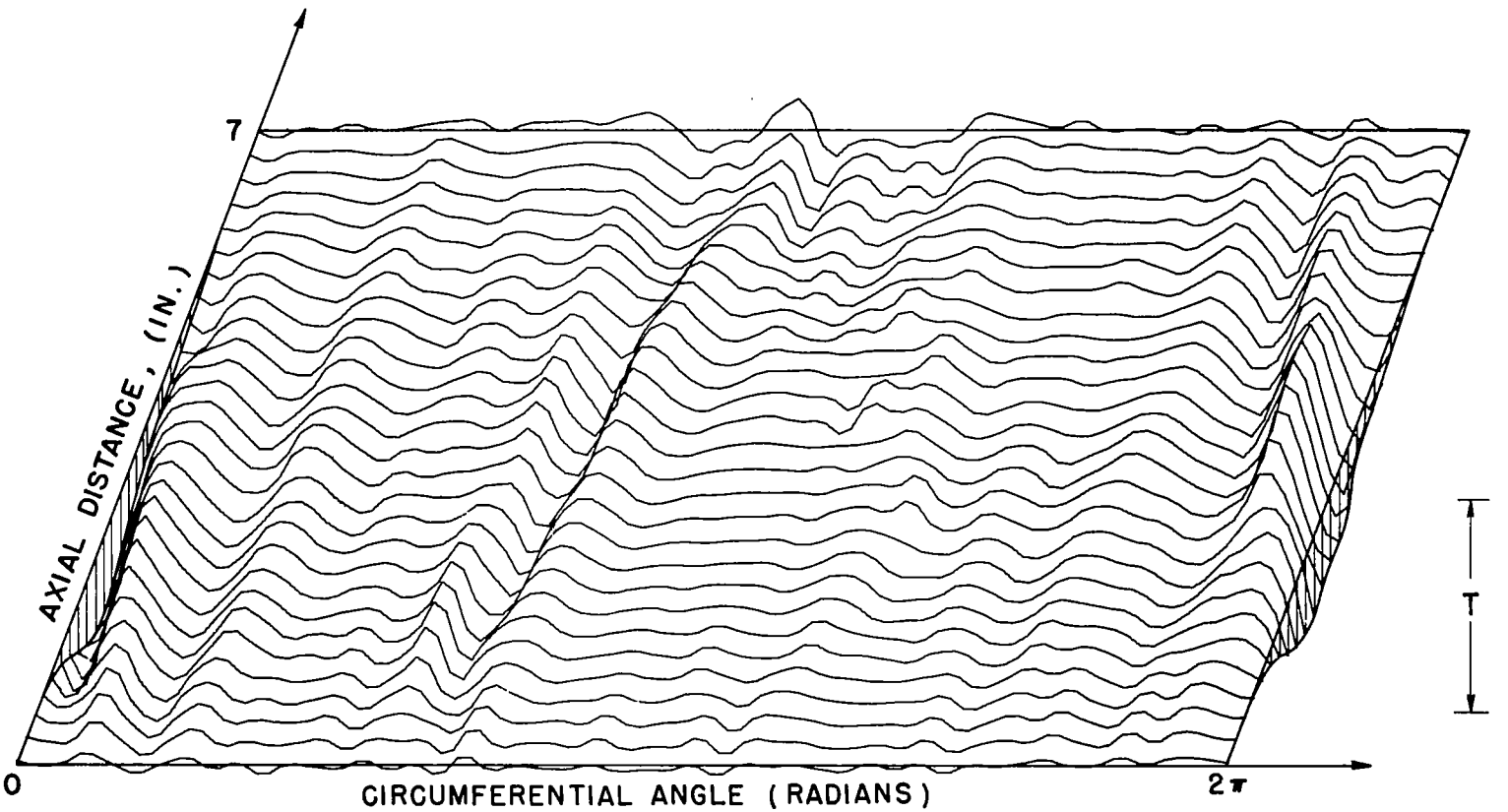

FIG. 32 PREBUCKLING DEFORMATION GROWTH AT $P/P_{CL} = 0.722$, SHELL A-9

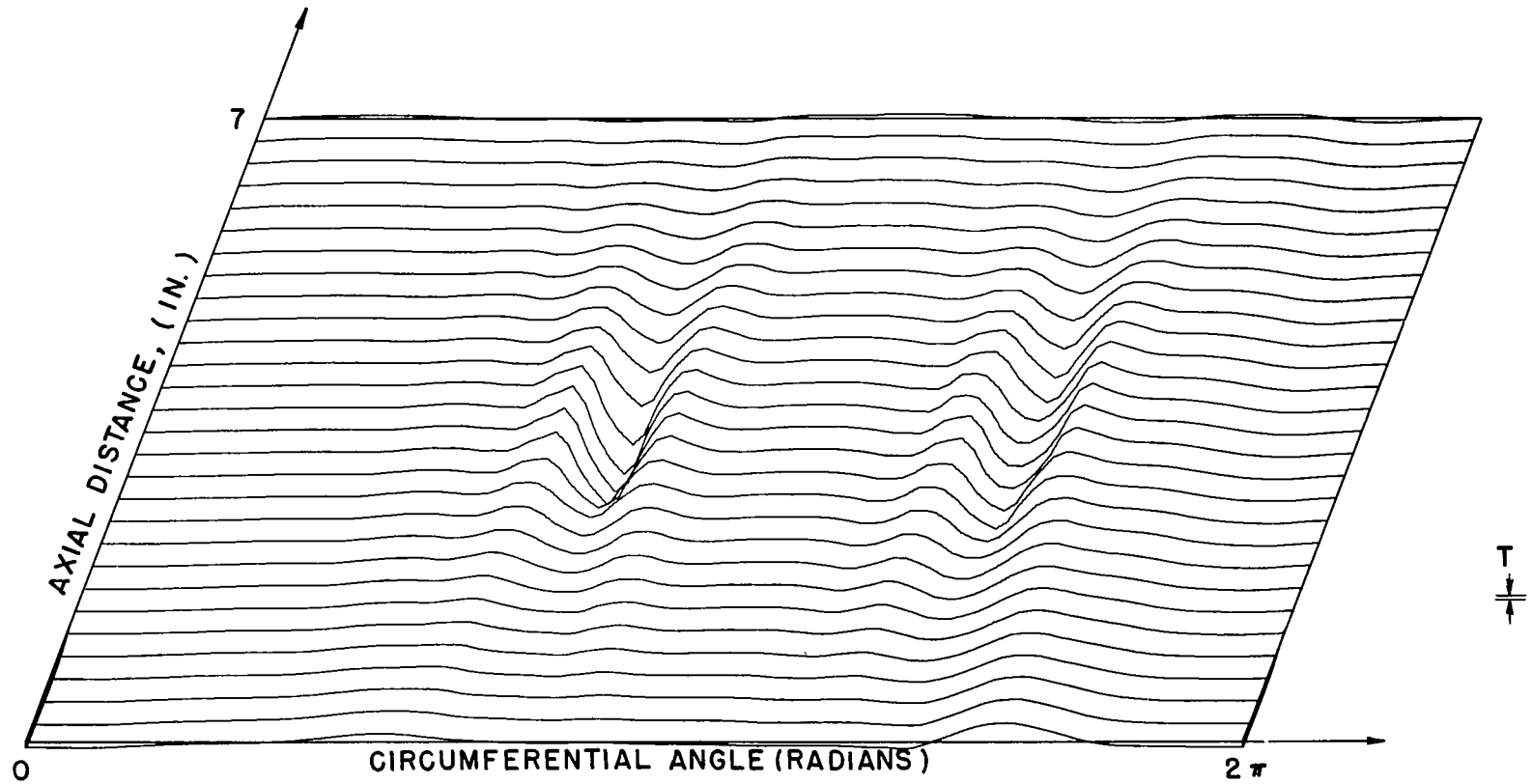

FIG.33 LOCAL BUCKLING DEFORMATION, SHELL A-7

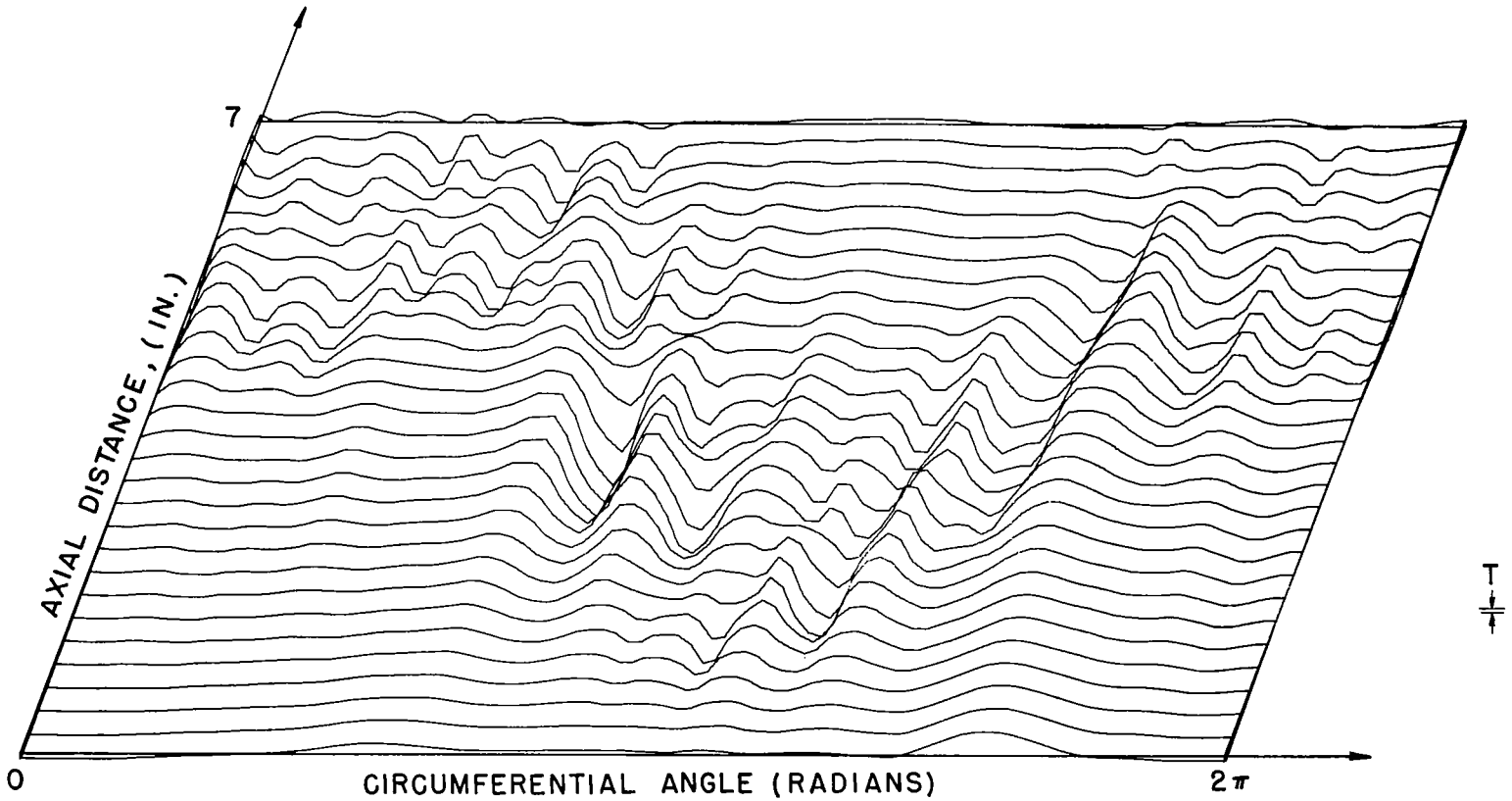

FIG. 34 POST BUCKLING DEFORMATION, SHELL A-7

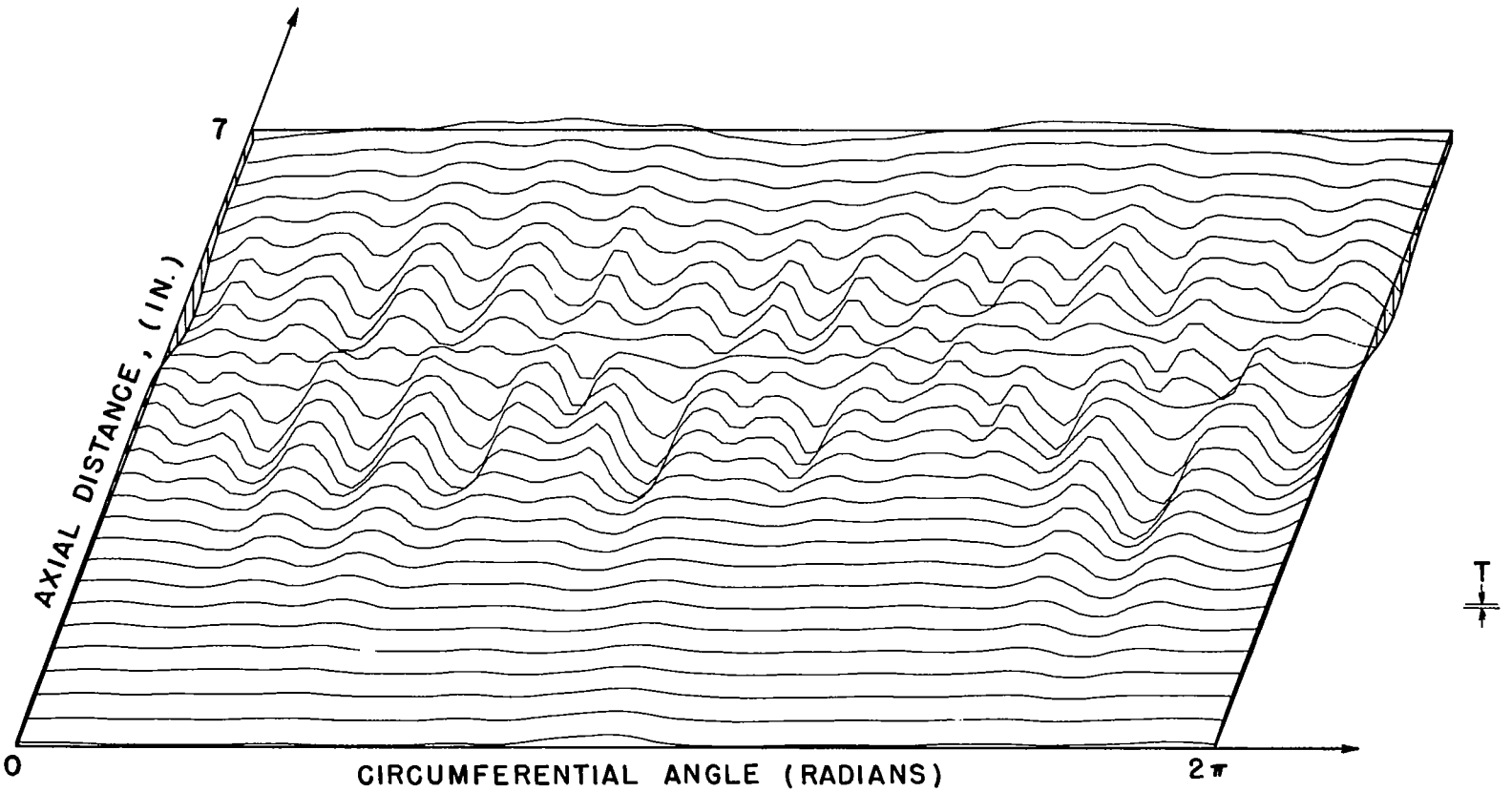

FIG.35 POSTBUCKLING DEFORMATION, SHELL A-8

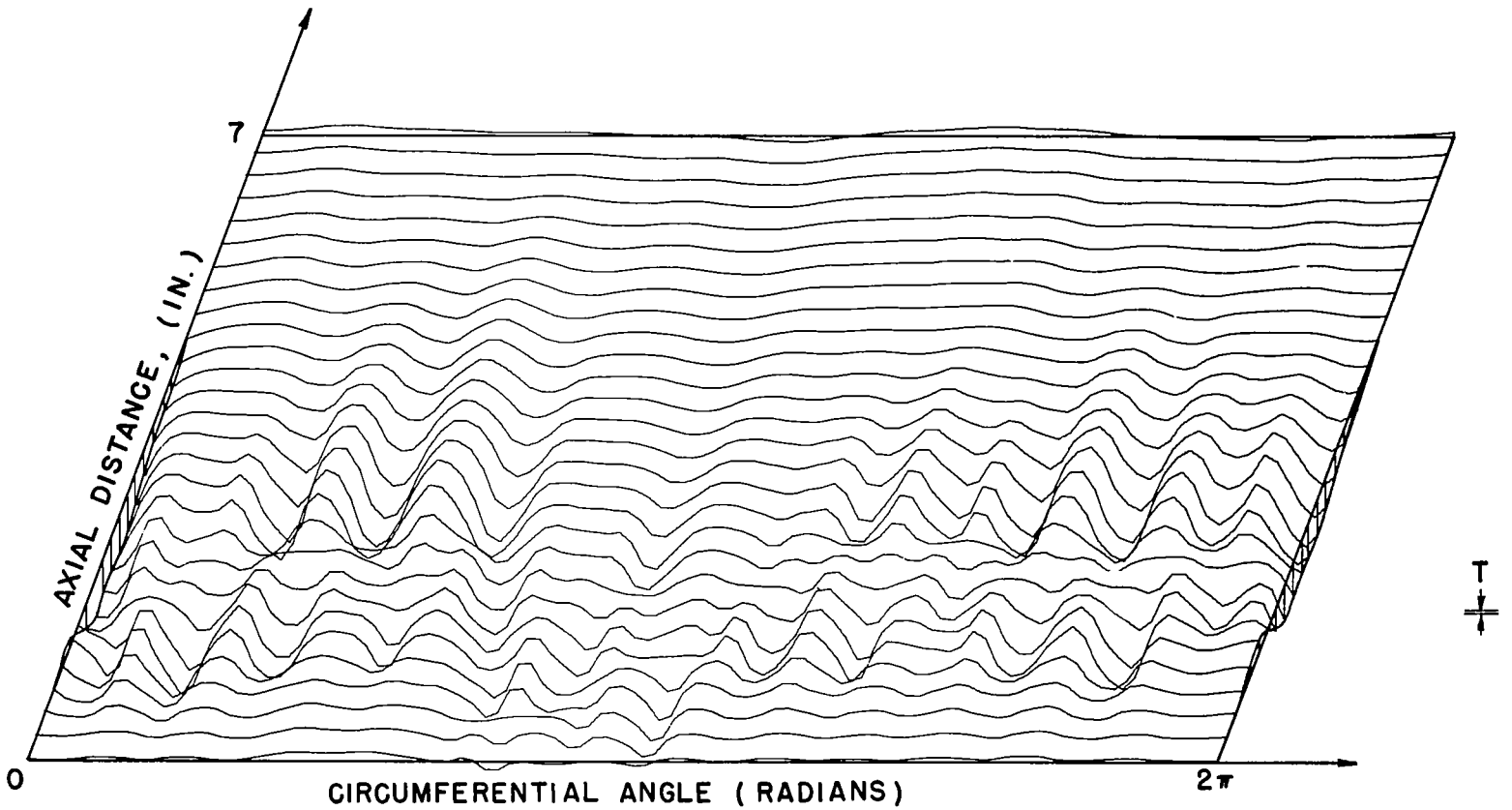

FIG. 36 POSTBUCKLING DEFORMATION, SHELL A - 9

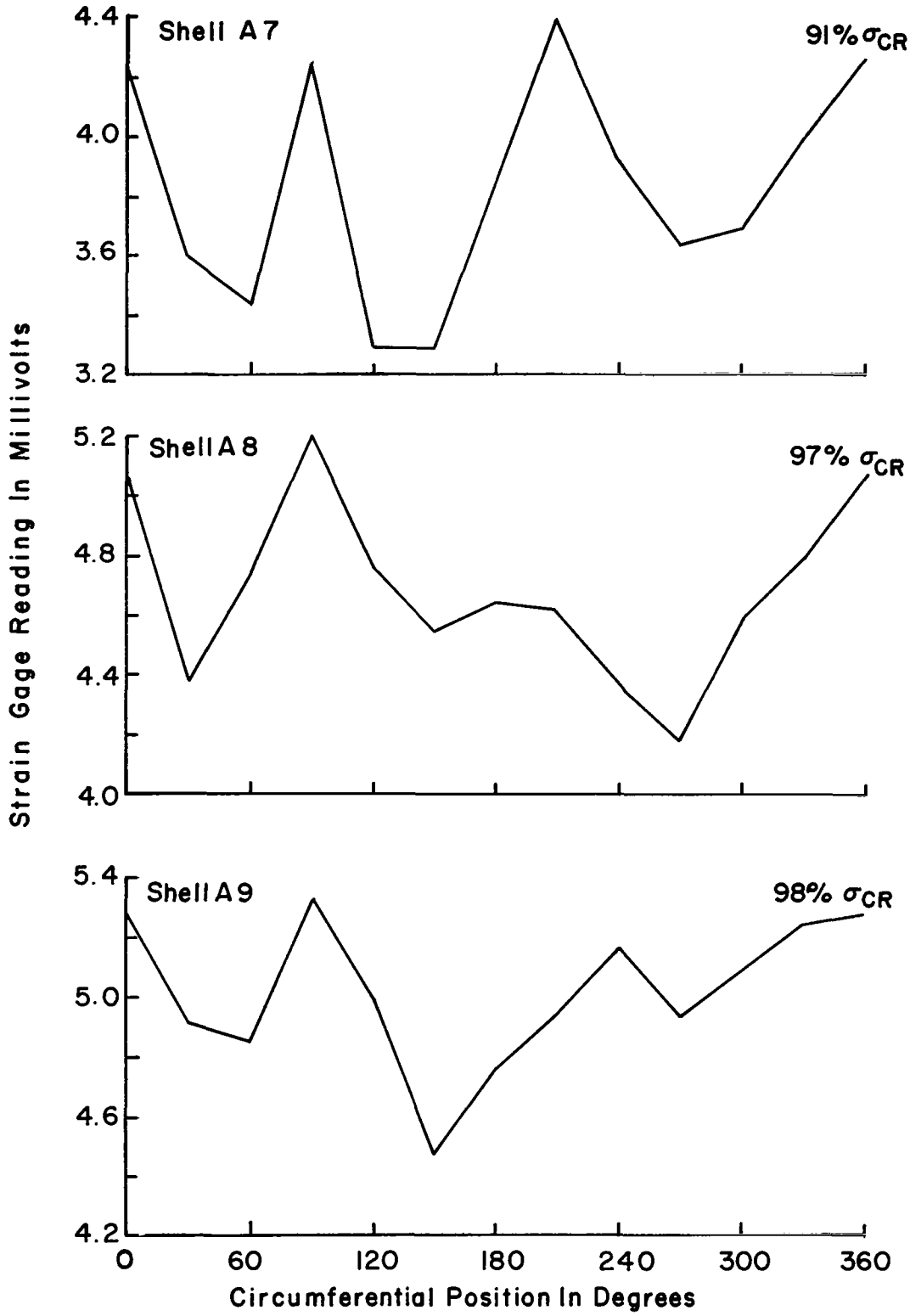

FIG.37 LOAD DISTRIBUTION NEAR BUCKLING

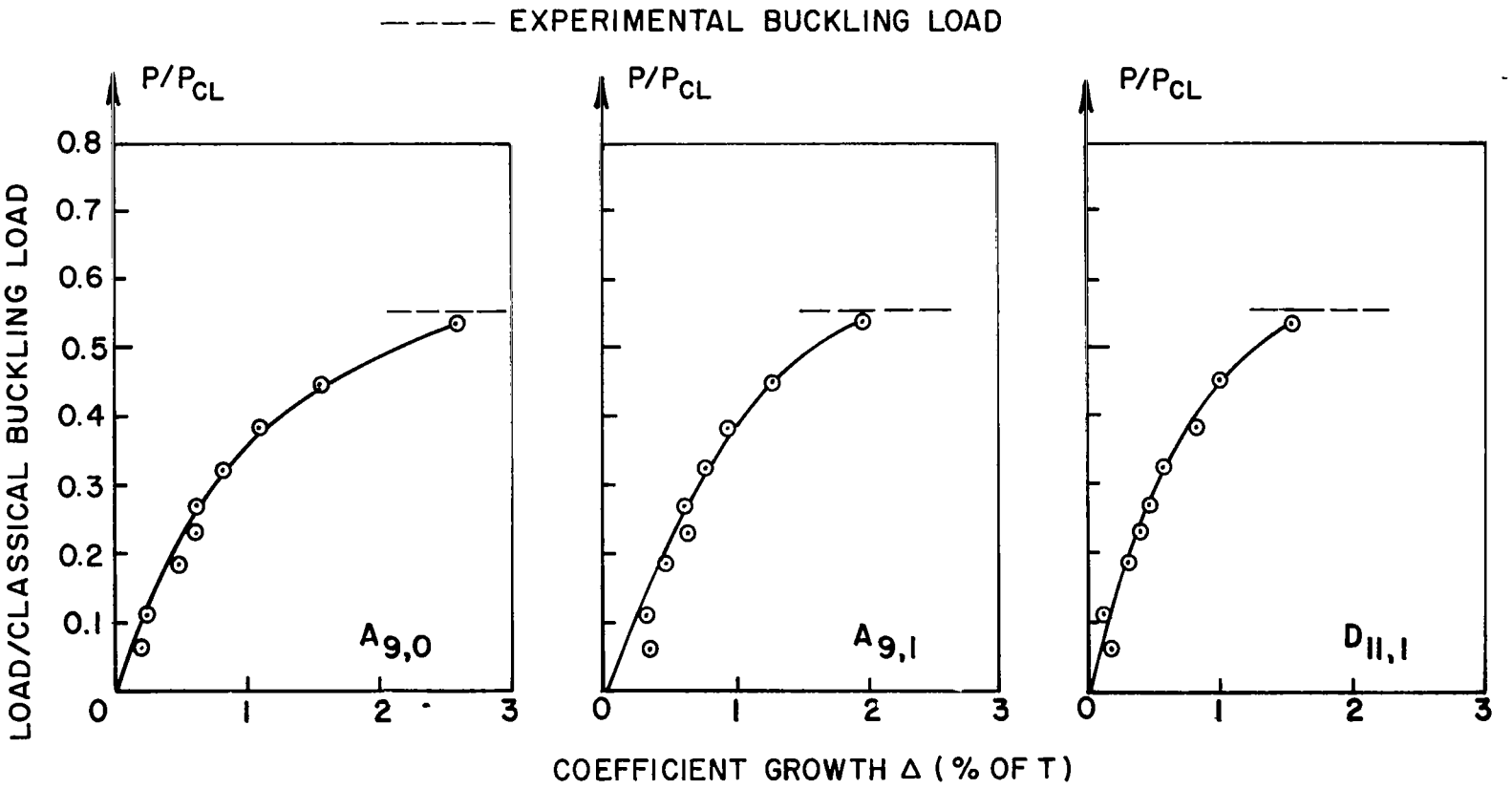

FIG. 38 GROWTH OF FOURIER COEFFICIENT FOR SHELL A-7

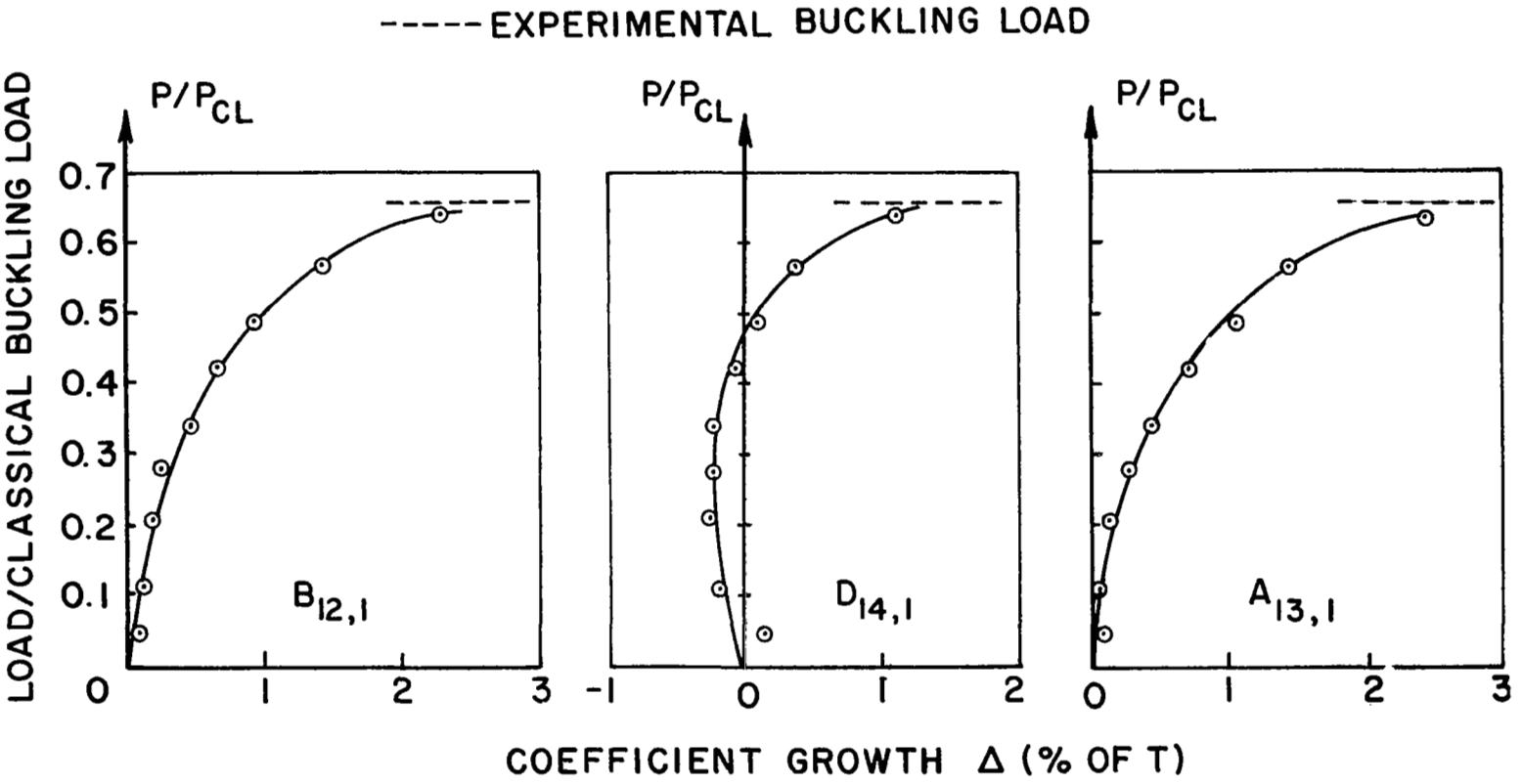

FIG. 39 GROWTH OF FOURIER COEFFICIENT FOR SHELL A-8

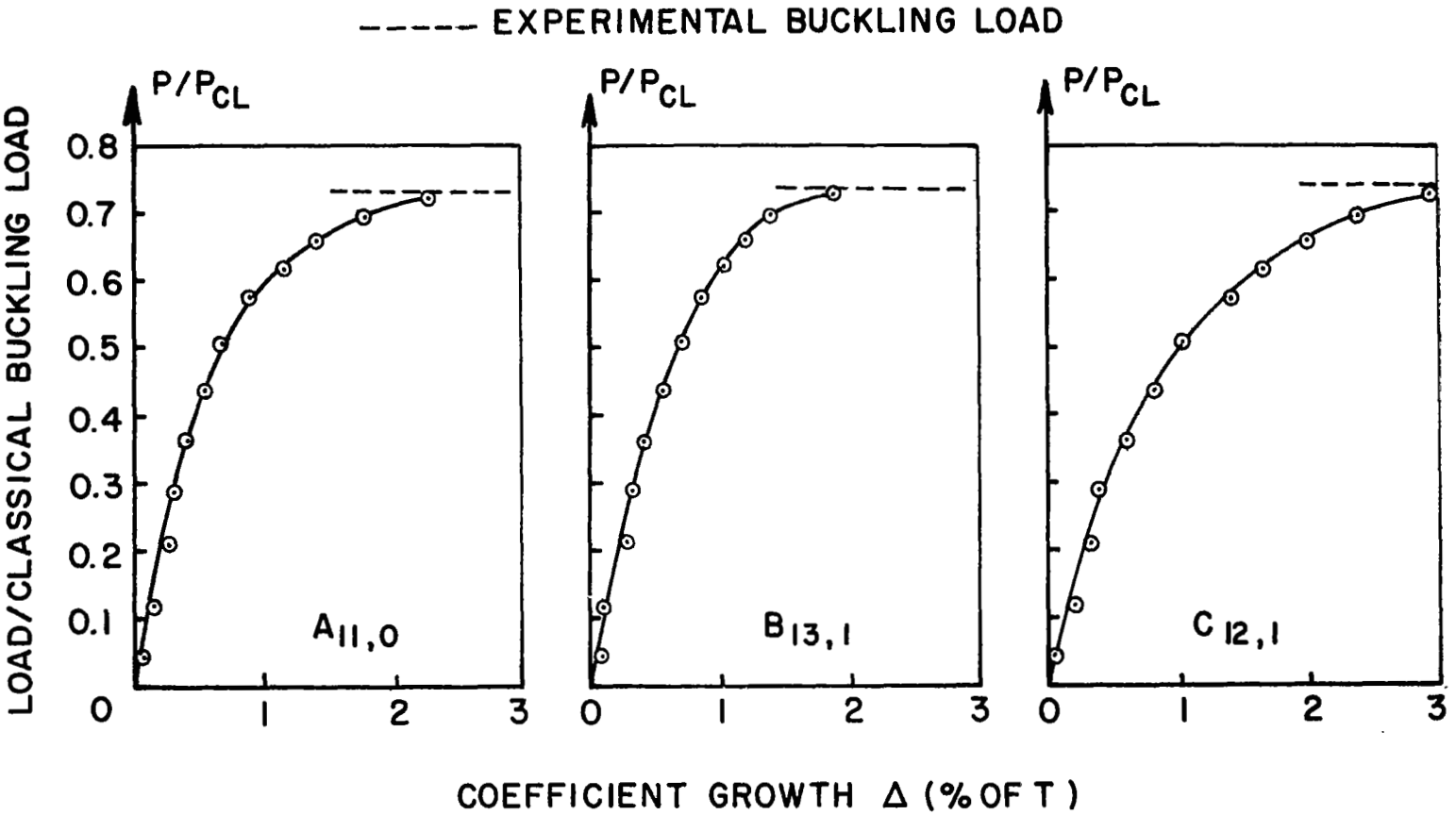

FIG. 40 GROWTH OF FOURIER COEFFICIENT FOR SHELL A-9